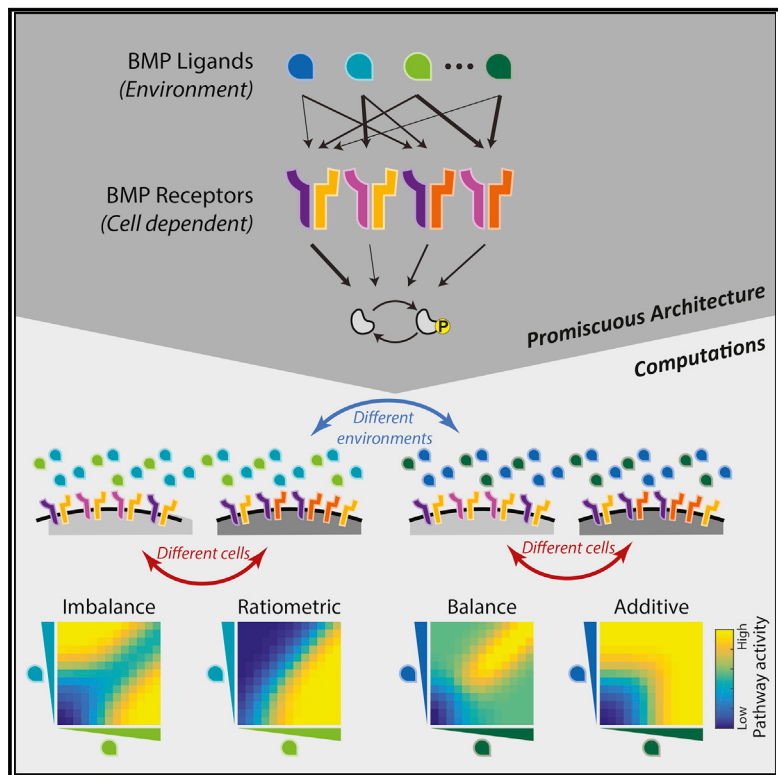


Combinatorial Signal Perception in the BMP Pathway

Graphical Abstract



Authors

Yaron E. Antebi, James M. Linton,
Heidi Klumpe, ..., Christina Su,
Reed McCardell, Michael B. Elowitz

Correspondence

melowitz@caltech.edu

In Brief

By harnessing promiscuous receptor-ligand interactions in the BMP pathway, a single cell can perform different computations, depending on which combinations of receptors and ligands are present.

Highlights

- Cells perform complex computations on combinations of BMP ligands
- A mathematical model shows how computations arise from receptor-ligand promiscuity
- A single cell type can perform different computations on different ligand pairs
- Changes in receptor profiles can reprogram the computations

Combinatorial Signal Perception in the BMP Pathway

Yaron E. Antebi,¹ James M. Linton,¹ Heidi Klumpe,^{1,2} Bogdan Bintu,¹ Mengsha Gong,¹ Christina Su,¹ Reed McCardell,¹ and Michael B. Elowitz^{1,3,4,*}

¹Division of Biology and Biological Engineering, California Institute of Technology, Pasadena, CA 91125, USA

²Division of Chemistry and Chemical Engineering, California Institute of Technology, Pasadena, CA 91125, USA

³Howard Hughes Medical Institute and Department of Applied Physics, California Institute of Technology, Pasadena, CA 91125, USA

⁴Lead Contact

*Correspondence: melowitz@caltech.edu

<http://dx.doi.org/10.1016/j.cell.2017.08.015>

SUMMARY

The bone morphogenetic protein (BMP) signaling pathway comprises multiple ligands and receptors that interact promiscuously with one another and typically appear in combinations. This feature is often explained in terms of redundancy and regulatory flexibility, but it has remained unclear what signal-processing capabilities it provides. Here, we show that the BMP pathway processes multi-ligand inputs using a specific repertoire of computations, including ratio-metric sensing, balance detection, and imbalance detection. These computations operate on the relative levels of different ligands and can arise directly from competitive receptor-ligand interactions. Furthermore, cells can select different computations to perform on the same ligand combination through expression of alternative sets of receptor variants. These results provide a direct signal-processing role for promiscuous receptor-ligand interactions and establish operational principles for quantitatively controlling cells with BMP ligands. Similar principles could apply to other promiscuous signaling pathways.

INTRODUCTION

Many intercellular signaling pathways, such as bone morphogenetic protein (BMP), Wnt, Notch, and JAK-STAT, exhibit a curious feature. Rather than using a single ligand and receptor, these systems comprise multiple ligand and receptor variants that interact promiscuously with one another to combinatorially generate a large set of distinct signaling complexes. These complexes activate the same intracellular targets and therefore appear to operate redundantly. Previous work has suggested that the use of redundant ligands and receptors offers regulatory flexibility (Llimargas and Lawrence, 2001) or provides robustness to genetic variation (Dudley and Robertson, 1997; Edson et al., 2010). However, it is also possible that this apparent redundancy provides specific signal-processing capabilities (Mueller and Nickel, 2012; Murray, 2007; Schmierer and Hill, 2007; Wodarz and Nusse, 1998).

The BMP pathway is an ideal example of promiscuous receptor-ligand architecture (Figure 1A). In mammalian species, it

includes more than 20 distinct ligands, 4 type I receptors (BMPR1A, BMPR1B, ACVR1, and ALK1), and 3 type II receptors (BMPR2, ACVR2A, and ACVR2B). These components could interact combinatorially to form hundreds of distinct receptor-ligand signaling complexes, each composed of 2 type I and 2 type II receptors binding a dimeric ligand. Active signaling complexes phosphorylate SMAD1, 5, and 8, which, together with SMAD4, translocate to the nucleus to regulate target gene expression (Heldin et al., 1997; Massagué, 1998).

Two features of the BMP pathway suggest the possibility of more complex signal processing. First, in most contexts, multiple BMP ligands and receptors appear in overlapping spatiotemporal distributions and therefore appear to be utilized in combinations (Danesh et al., 2009; Faber et al., 2002; Lorda-Diez et al., 2014; Salazar et al., 2016). For example, BMP9 and BMP10 co-regulate the formation of vasculature (Chen et al., 2013; Ricard et al., 2012), while BMP2, BMP4, GDF5, and GDF6 operate together in joint development (Storm and Kingsley, 1996). Similarly, at least 6 distinct ligands and 3 receptors are involved in kidney development (Simic and Vukicevic, 2005). Second, individual ligands preferentially signal through particular receptors. For example, ALK1 is preferentially activated by BMP9 and BMP10 in endothelial cells (David et al., 2007); GDF5 signals mainly through BMPR1B and not BMPR1A (Nishitoh et al., 1996); and BMP2/4 and BMP6/7 signal through distinct receptors to induce mesenchymal stem cell differentiation (Lavery et al., 2008).

The ability to form many competing complexes with distinct affinity and activity preferences could, in principle, allow the system to perform complex signal processing. However, we lack a general quantitative framework to understand how the BMP pathway perceives combinations of ligands, how such combinatorial perception emerges from underlying molecular interactions, and whether and how distinct cell types respond differently to the same ligand combinations.

Here, combining theoretical and experimental approaches, we show that the BMP pathway perceives ligand combinations through a specific family of multi-dimensional response profiles. These profiles allow the pathway to perceive relative, in addition to absolute, levels of multiple ligands. Mathematical modeling further reveals that these response profiles can arise from interplay between receptor-ligand binding affinities and the quantitative activity of each complex. The former determine what complexes are formed, while the latter determines how the activities of those complexes combine to establish overall

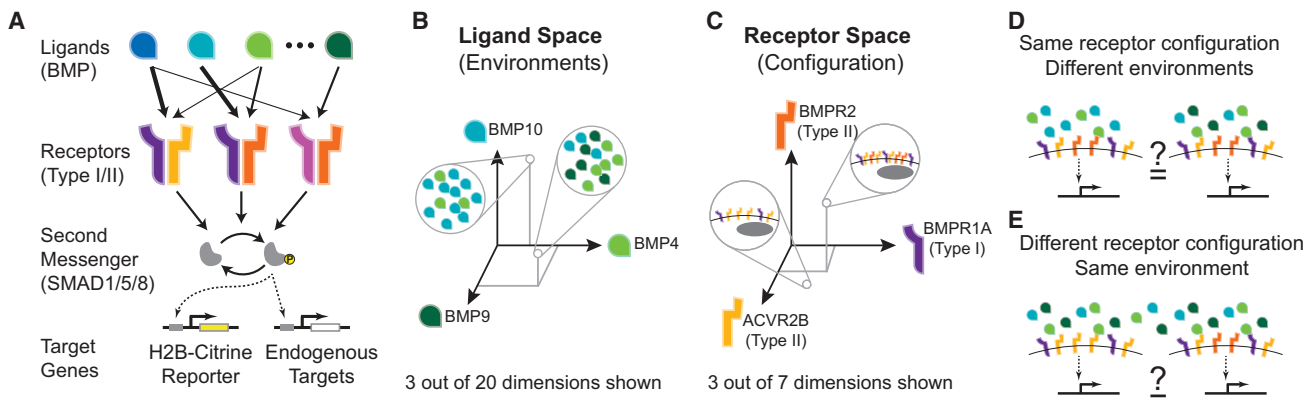


Figure 1. Promiscuous Receptor-Ligand Interactions Can Be Analyzed in Terms of Multi-dimensional Ligand and Receptor Spaces

(A) In the BMP signaling pathway, multiple ligand variants (blue and green) interact promiscuously with multiple distinct type I (orange and yellow) and type II (purple and pink) receptor heterodimers. Most ligands interact with multiple receptor complexes (arrows), but all active signaling complexes phosphorylate the same second messenger, SMAD1/5/8. Phosphorylated SMAD1/5/8, in complex with SMAD4, activates endogenous targets (white) and a stably integrated fluorescent reporter gene (yellow).

(B and C) Cellular environments and expression levels can be represented as points in multi-dimensional spaces. (B) Ligand concentration space represents the possible local environments of cells. Only 3 ligands are plotted for simplicity, but the full space includes dimensions for each ligand species. Zoomed circles indicate examples of two environments with distinct concentrations of ligands. (C) Receptor space represents the space of possible receptor expression profiles. Only 3 of 7 dimensions are shown. Two example cell types with distinct receptor expression profiles are indicated (circles).

(D and E) These representations provoke the questions of how multiple ligands combine to determine pathway activity in a given cell type (D) and how different cell types respond to the same ligand combination (E).

pathway activity. Critically, we find that the response profiles differ qualitatively and quantitatively depending on the expression levels of the different receptor variants. As a result, different cell types, with distinct receptor expression profiles, can respond to distinct features in the multidimensional space of ligand concentrations. Together, these results establish a general framework for analyzing the BMP signaling pathway and reveal a more general design principle for biological signaling systems containing promiscuous receptor-ligand interactions.

RESULTS

Theoretical Framework

To analyze the way in which the BMP pathway uses multiple receptor variants to integrate signals from multiple dimeric ligand species, it is useful to consider two multi-dimensional spaces. Cellular environments, specified by the concentrations of each of the dimeric ligand species, can be represented as points in a multi-dimensional “ligand space” (Figure 1B). Similarly, individual cell types typically co-express multiple type I and type II receptors (Cheifetz, 1999) and can therefore be represented as points in a 7-dimensional “receptor space” specified by the individual expression levels of each receptor (Figure 1C). (This space is, more precisely, the combination of a 3-dimensional space for the type I receptors and a 4-dimensional space for the type II receptors.) Not every point in ligand or receptor space may be realized biologically, and other secreted and intracellular factors further modulate BMP signaling in specific contexts (Balemans and Van Hul, 2002; Zakin and De Robertis, 2010). Nevertheless, understanding signal processing by the BMP pathway requires determining

how multiple ligands combine, or integrate, to control the pathway activity in a cell with a given receptor configuration (Figure 1D) and whether distinct cells, expressing specific combinations of receptors, can integrate the same ligands in qualitatively different ways (Figure 1E).

BMP Ligands Exhibit Combinatorial Effects

In order to address these questions experimentally, we set out to measure the dependence of BMP pathway activity on individual ligands and ligand combinations. Ligand monomers form covalent homodimers and heterodimers with distinct activities (Israel et al., 1996; Neugebauer et al., 2015; Valera et al., 2010). Here, we focused on mixtures of distinct homodimeric ligands, which have been shown to produce non-additive responses in some systems (Ying et al., 2000, 2001; Ying and Zhao, 2001; Açıklı et al., 2014). Mixtures of heterodimeric ligands could be analyzed similarly.

To quantitatively measure BMP pathway activity, we constructed a reporter cell line by stably integrating a histone 2B (H2B)-Citrine fluorescent reporter driven by a BMP response element (BRE) specific for SMAD1/5/8 (Korchynskyi and ten Dijke, 2002) into the NAMRU mouse mammary gland (NMuMG) epithelial cell line, in which the BMP pathway can be activated without inducing differentiation (Piek et al., 1999). Reporter expression correlated with phosphorylation of SMAD1/5/8 and with endogenous BMP target gene expression (Figures S1A–S1C) and exhibited a unimodal distribution for each ligand concentration (Figure S1D). After an elevated transient response to BMP addition, pSMAD levels reached a steady state within 90 min (Figure S1E). The steady-state behavior was also reflected in reporter fluorescence, which accumulated at an approximately constant rate over time for up to 48 hr (Figure S1F).

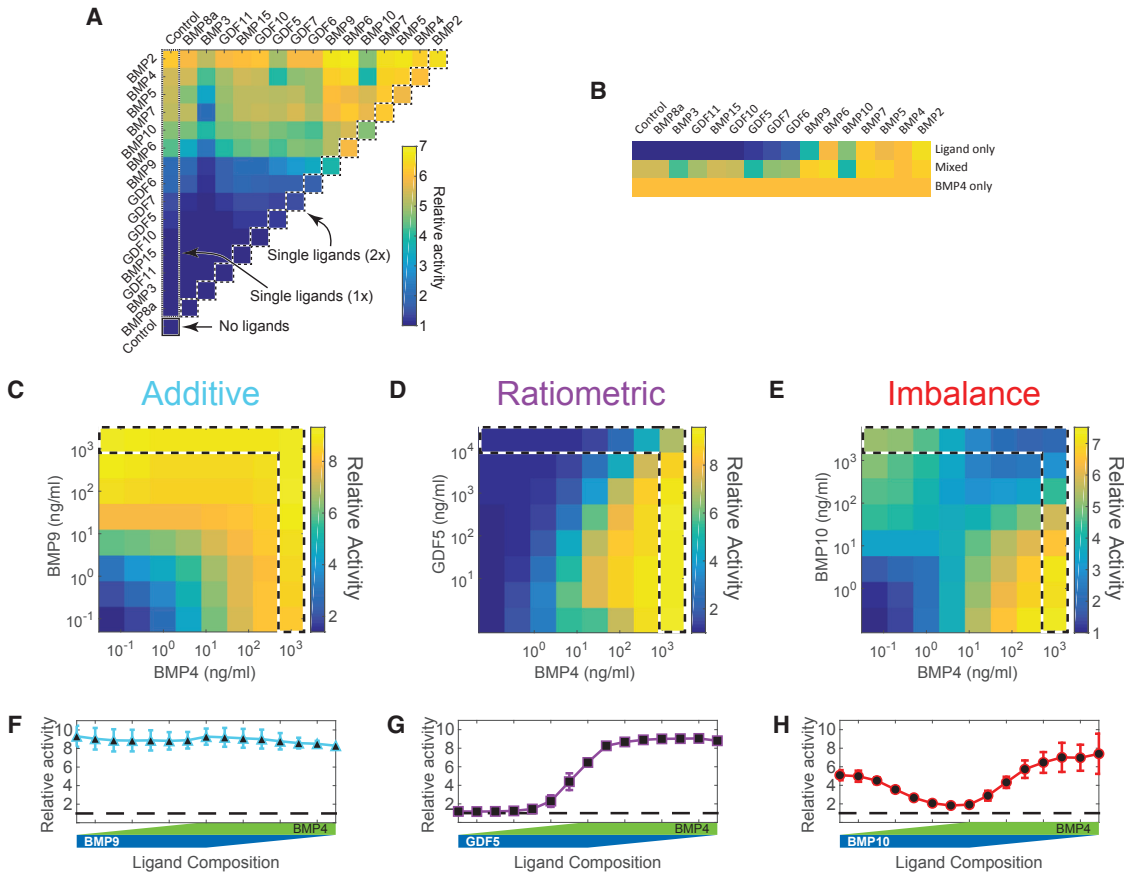


Figure 2. The BMP Pathway Perceives Ligand Combinations

(A) NMuMG reporter cells were exposed to 136 different combinatorial pairings of 15 homodimeric BMP ligands, as indicated. Color scale indicates mean fluorescence level at 24 hr, normalized by the uninduced population (relative activity).

(B) From the complete interaction matrix, we extracted the individual response to each ligand (top row) and compared to the response to BMP4 (bottom row) and to mixtures of each ligand with BMP4 (middle row). By comparing each vertical triplet, we see that specific ligands combine with BMP4 in different ways, both synergistically and antagonistically.

(C–E) Measurements of full input-output response profiles for specific ligand pairs. BMP4 and BMP9 combine to increase pathway activity in an additive fashion (C). BMP4 and GDF5 combine in a ratiometric manner (D). BMP4 and BMP10 showed an “imbalance detection” response (E). For each plot in (C–E), the dashed outline indicates a set of ligand concentrations varying from high concentration of one ligand (top left corner) to high concentration of the other ligand through intermediate states containing both ligands (e.g., top right). In (C–E), the bottom row and left column correspond to an absence of the indicated ligand.

(F–H) The responses along the dashed contour are plotted for BMP4-BMP9 (F), BMP4-GDF5 (G), and BMP4-BMP10 (H). Each pair shows a different dependence on ligand ratio. The logarithmic levels of each ligand are indicated schematically by the heights of the blue/green bars along the x axis. Error bars indicate SD calculated from at least 3 experiments.

See also Figures S1 and S2 and Tables S1 and S4.

(Since the fluorescent protein is stable and the cell cycle is longer than 24 hr in these conditions, linear accumulation indicates a constant rate of reporter expression.) Based on these dynamics, we selected 24 hr post induction as a time point for subsequent analysis.

As a first step to classifying ligand integration behaviors, we sought to identify candidate ligand pairs for subsequent higher-resolution analysis. We performed a coarse-grained survey of 15 commercially available homodimeric ligands (Figure 2A). We measured reporter expression in response to each ligand individually, at a specific base concentration (STAR Methods; Table S1); each ligand at twice its base concentration (diagonal elements); and each pair of ligands at their base

concentrations (other matrix elements). To quantify pathway activity, we normalized each measurement by basal activity with no added ligand (bottom).

Many individual ligand pairs generated stronger or weaker responses than expected given their individual effects (Figures 2A, S1G, and S1H). For example, BMP3 combined antagonistically with almost every other ligand. Furthermore, some individual ligands combined in qualitatively different ways with different ligands. For example, BMP7 and BMP4 each exhibited a mixture of antagonistic and synergistic interactions with other ligands. Overall, these results indicate that the effect of any given ligand on pathway activity can, in general, depend in complex ways on other ligands.

Higher-Resolution Analysis Reveals Distinct Multi-ligand Response Profiles

To gain a clearer view of multi-ligand responses, we analyzed the diverse ways in which BMP4, one of the best-studied BMP ligands, combines with other ligands (Figure 2B), particularly BMP9, GDF5, and BMP10 (Figures 2C–2E). To quantitatively characterize these interactions in a manner independent of the choice of base concentrations, we analyzed a 2-dimensional matrix of logarithmically spaced ligand concentrations (Figures 2C–2E). The broad (3 orders of magnitude) concentration range covers the full input dynamic range for each ligand pair in the NMuMG cell line and overlaps ligand concentrations in circulating blood (David et al., 2008), as well as those used to induce BMP-dependent responses *in vitro* (Lavery et al., 2008; Heggebø et al., 2014; Hatsell et al., 2015).

Each of the three ligand pairs showed qualitatively distinct response profiles. BMP4 and BMP9 increased pathway activity both individually and in combination, exhibiting an additive response, with little dependence on ligand identity, as one would expect for ligands that function redundantly (Figures 2C and S2A). By contrast, GDF5 reduced activation by BMP4 in a dose-dependent fashion, such that pathway output approximated the ratio of the concentrations of the two ligands (Figures 2D and S2A). Similar ratiometric responses have been observed in other systems (Atkinson, 1968; Berg et al., 2009; Escalante-Chong et al., 2015; Madl and Herman, 1979). Finally, and most intriguingly, BMP4 and BMP10 were potent activators individually, but each became inhibitory in the presence of high concentrations of the other ligand, resulting in a weaker response when both ligands were present (Figures 2E and S2A). Interestingly, in this mode, each ligand can play both activating and inhibitory roles. We termed this integration mode “imbalance detection,” because it responds maximally to extreme ratios (imbalances) of the two ligand concentrations. We note that the same 2-dimensional response profiles were observed using independently generated reporter cell lines, indicating that they do not reflect aspects of the chromatin configuration of a specific reporter integration site (Figure S2C). The integration functions were also independent of the ligand supplier (Figure S2D). Together, these results identify three distinct ways in which the BMP pathway can integrate ligand pairs.

Interestingly, these responses depend in distinct ways on the ligand composition, defined as the relative concentrations of the two ligands. To study this dependence, we plotted the response to varying relative ligand concentrations at high total ligand concentration (Figures 2C–2E, dashed outline). These contours reveal that pathway activity is independent of ligand composition in the additive case (Figure 2F), monotonically dependent in the ratiometric case (Figure 2G), and non-monotonically dependent in the imbalance detection case, where pathway activity declines near a specific intermediate ligand ratio (Figure 2H). Similar composition dependence can be observed at lower ligand concentrations. The only exception is imbalance detection, which at ligand concentrations <10 ng/mL becomes indistinguishable from the additive response (Figure 2C). These results indicate that the BMP pathway implements a diverse set of computations on multi-ligand inputs in NMuMG cells and can be strongly

controlled by ligand composition, as well as absolute ligand concentration.

Response Profiles Emerge Rapidly and Are Stable

We next asked at what level and over what timescales these response profiles emerge. First, to access an earlier and more direct readout of pathway activity, we measured SMAD1/5/8 phosphorylation at 20 min after stimulation with select ligand pairs, using immunostaining (Figure 3A) and western blots (Figures S2E and S2F). Both measurements revealed qualitatively similar response profiles as the fluorescent reporter, indicating that computations emerge within 20 min and can be observed at the level of SMAD phosphorylation. We note that ERK1/2, a non-canonical output (Nohe et al., 2004), did not respond to BMP stimulation in this cell context (Figure S2G).

Next, to better understand the dynamics of the BMP response, we used time-lapse imaging to track reporter expression over time in response to BMP4 and/or BMP10 (Figures 3B and S3A). The imbalance detection response could be identified by 6 hr and persisted for more than 96 hr. However, the relative level of activation caused by the combination of BMP4 and BMP10, compared to the individual ligands, remained constant (Figure S3B), indicating that the imbalance detection response profile is stable over extended periods.

Feedback Loops and Pathway Modulators

We next asked whether known feedback loops in the BMP pathway were necessary for the observed computations. The negative pathway regulator SMAD6 is a downstream target of BMP (Figure S1B) (Li et al., 2003; Afrakhte et al., 1998). However, knockdown of SMAD6 did not qualitatively change the shape of the response profiles (Figures S3C–S3E). Another reported feedback involves upregulation of BMPR2 in response to BMP9 stimulation (Long et al., 2015). Addition of 400 ng/ml BMP9 generated a 2-fold increase in BMPR2 expression (Figure S3F). However, even this relatively modest effect appeared only at ~12 hr, consistent with the timescales of transcriptional regulation and too late to explain the appearance of the computations at earlier time points. These results suggest that these feedback loops are not required for the computations observed here, although feedbacks may play other roles in enhancing the amplitude or dynamics of the pathway over longer timescales.

The BMP pathway utilizes many secreted and surface-bound modulators to shape the spatial distribution of available ligands. To test whether these factors play a role in ligand integration, we first determined which ones were expressed in the NMuMG cell line (Table S2). Individually depleting each of these factors using siRNAs (Figure 3C) did not affect the type of response profile generated by BMP4 in combination with BMP9, BMP10, or GDF5 (Figures 3D–3G). In addition, BMPs could interact more generally with heparan sulfate proteoglycans (HSPGs). Enzymatically perturbing HSPGs with heparinase or inhibiting their biosynthesis with NaClO₃ showed minimal effects on the response of the pathway to BMP combinations (Figures S3G–S3J). Together, these results suggest that while these modulators play key roles in other aspects of BMP signaling, they are not required for the observed multi-ligand

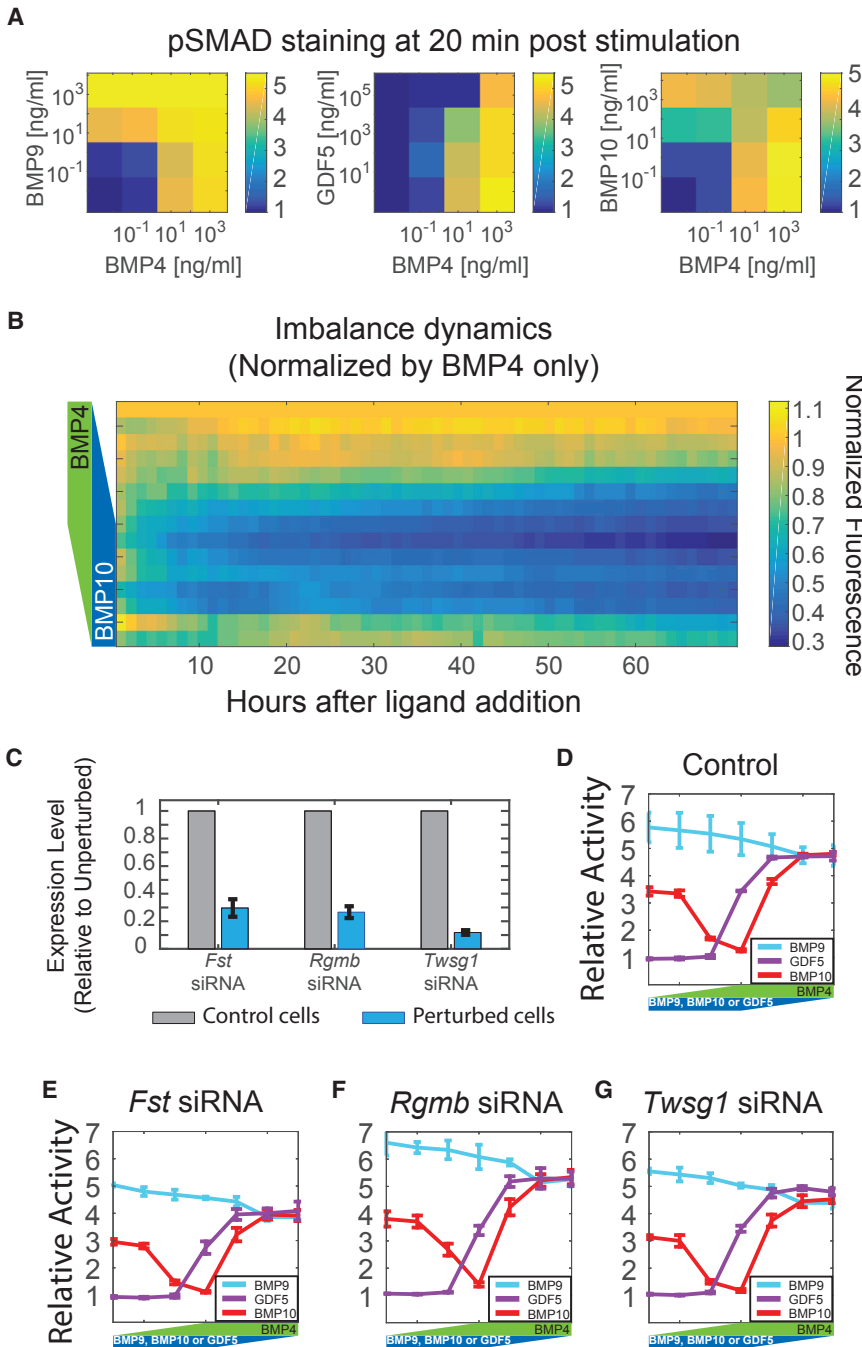


Figure 3. Combinatorial Ligand Response Profiles Emerge Rapidly, Persist for Long Periods, and Do Not Require Co-factors

(A) Phospho-SMAD immunostaining reveals responses to BMP4-BMP9, BMP4-GDF5, and BMP4-BMP10 ligand combinations 20 min after ligand addition. Colors indicate pSMAD levels relative to unactivated cells.

(B) The dynamical response to mixtures of BMP4 and BMP10 is plotted over 70 hr after addition of the ligands. Data are normalized at each time point to the response of cells treated with BMP4 only.

(C) Expressed BMP modifiers, identified in RNA sequencing (Table S2), were depleted from NMuMG using siRNA. The relative expression levels of *Fst*, *Rgmb*, and *Twsg1* were measured using qPCR in cells transfected with the corresponding siRNA (blue) normalized to their levels in cells transfected with a random siRNA (gray).

(D–G) After depletion by random siRNA (D), *Fst* siRNA (E), *Rgmb* siRNA (F), or *Twsg1* siRNA (G), cells were treated with varying levels of BMP4 and the indicated ligand to assess their potential effect on combinatorial ligand response profiles. In (C)–(G), error bars indicate SD calculated from three independent experiments. See also Figures S2 and S3 and Tables S2–S4.

computations. These results are, however, consistent with computations emerging directly from receptor-ligand interactions.

A Minimal Model of Promiscuous Receptor-Ligand Interactions

To understand how receptor-ligand interactions could generate the observed complex ligand integration modes, we constructed a simplified mathematical model that incorporates two key features of the BMP pathway: the bipartite structure of active

BMP receptor complexes (i.e., the requirement for both type I and type II receptors) and promiscuous, competitive receptor-ligand interactions (Figures 4A and 4B) (Heinecke et al., 2009; Massagué, 1998; Mueller and Nickel, 2012; Nickel et al., 2009; Vilar et al., 2006). The model considers a set of ligands, denoted L_j , and two types of receptors, denoted A_i and B_k , analogous to the BMP type I and type II receptor subunits, respectively. Each ligand can bind with affinity K_{ij}^D to an A-type receptor to form a dimeric complex, D_{ij} , which in turn can bind a B-type receptor with affinity K_{ijk}^T to form an active trimeric complex, T_{ijk} . Because the affinity parameters can differ for each ligand-receptor combination, this model allows both receptor preferences as well as promiscuous interactions. Each trimeric complex phosphorylates SMAD proteins at a

distinct rate, or activity, denoted ε_{ijk} , to produce an overall output signal S at the steady state. The model considers the experimental regime of large extracellular volume, but similar conclusions occur at finite volume (STAR Methods). Here, we focus on the minimal case of 2 ligands, 2 A-type receptors, and 2 B-type receptors, whose behavior can be specified by 16 independent biochemical parameters and 4 receptor expression levels and which is sufficient to explain the present experimental observations.

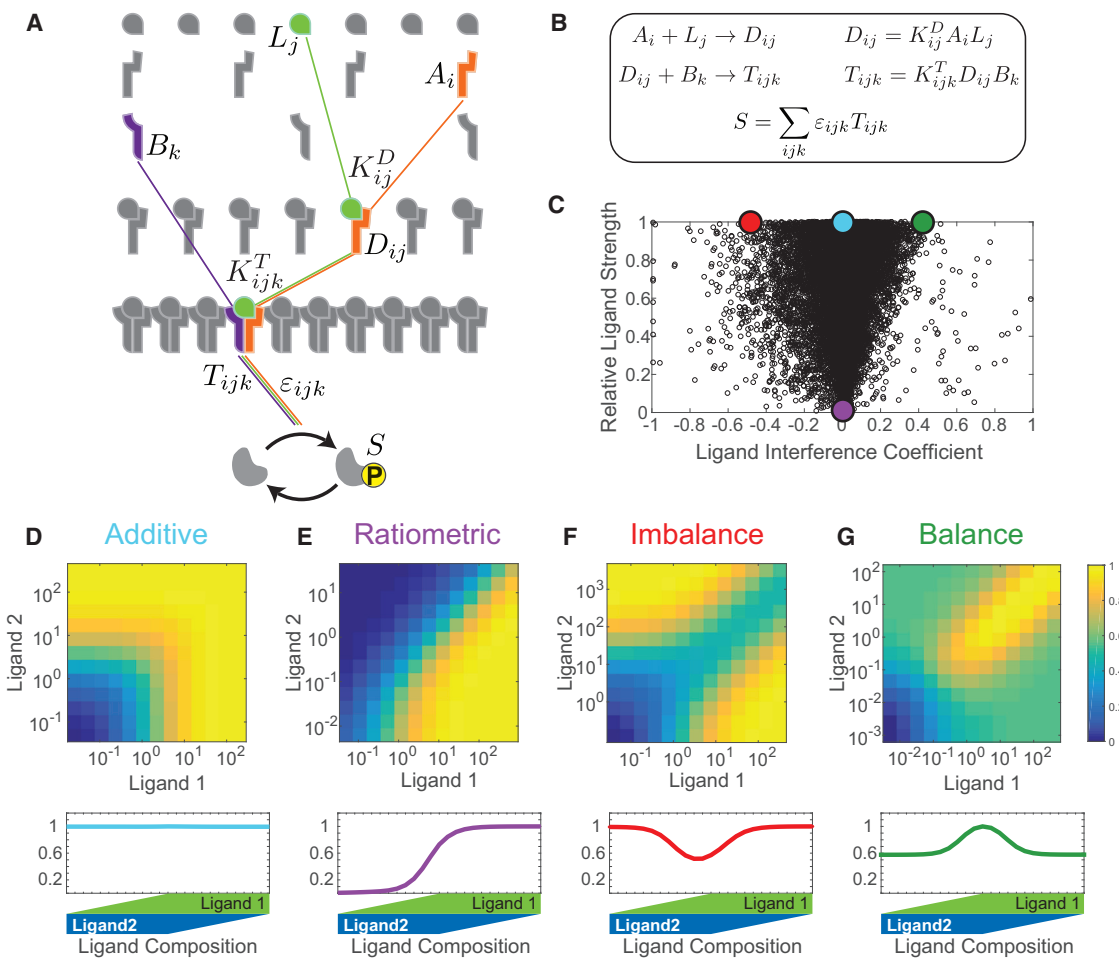


Figure 4. Mathematical Modeling Shows that Combinatorial Receptor-Ligand Interactions Generate a Specific Repertoire of Computational Functions

(A) Schematic representation of ligands (top row), type A receptors (second row), type B receptors (third row), intermediate complexes (fourth row), and signaling complexes (fifth row), as described in the text. Only a subset of possible complexes is shown for simplicity. Colored lines highlight interactions involved in the formation of a single signaling complex, with corresponding parameters indicated.

(B) Reactions (left), corresponding steady-state equations (right), and the equation for the total response (bottom) for the model.

(C) With 2 ligands and 2 variants of each receptor type, the model produces a variety of different signal-processing behaviors. Each point represents the behavior of one randomly chosen parameter set. The x axis represents the type and strength of interference between the ligands, from antagonism (negative values) to synergy (positive values). The y axis represents the relative strength of the two ligands individually, as defined in Figure S4B and STAR Methods. Most parameter sets generate computations that fall within a triangular region, while some show more extreme phenotypes. The four archetypal computations, shown in (D)–(G), are indicated by colored dots.

(D–G) The four archetypal computations (additive, [D]; ratiometric, [E]; imbalance, [F]; and balance, [G]) are shown (top) together with corresponding profiles showing pathway activity as a function of ligand ratio, as in Figures 2F–2H (bottom). Colors indicate normalized response strength. See also Figures S4 and S5.

This simplified model omits several known features of the BMP pathway, such as variations in the sequence of binding reactions (Gilboa et al., 2000; Rosenzweig et al., 1995; Ventura et al., 1995), the hexameric nature of actual signaling complexes, and the roles of other BMP regulatory factors. These features likely play important biological roles (e.g., controlling the amplitude and spatiotemporal dynamics of signaling) that should be considered in models of specific biological processes. However, incorporation of these additional features in the model does not change the types of input-output computations examined here (STAR Methods).

Archetypal Functions Define the Range of Response Profiles

To explore the range of integration modes produced by the model, we computed the input-output behavior of the system for 100,000 random parameter sets (Figure S4A). The model produced a repertoire of computational response profiles, which included additive, ratiometric, and imbalance detection. To more quantitatively characterize this repertoire, we defined two features that together capture key aspects of the shape of the response profiles (Figures S4B–S4D). First, we defined the relative ligand strength (RLS) to quantify the asymmetry in pathway

activity generated by the ligands individually. The RLS is defined as the ratio of pathway activity produced by the weaker ligand to that produced by the stronger ligand. Second, we defined the ligand interference coefficient (LIC) to quantify the degree to which the two ligands positively or negatively synergize (**STAR Methods**). The LIC is defined by the deviation of pathway activity in mixed ligand environments beyond the range of the responses in single ligand environments.

When plotted in this two-parameter phenotypic space, the simulated systems occupied a continuous region that loosely conformed to an inverted triangle (Figures 4C and S4E). Two vertices of the triangle strikingly resembled the ratiometric and imbalance detection functions observed experimentally (cf. Figures 2C–2E and Figures 4D–4F). The third vertex, occurring for ligands with a RLS of 1 and a positive LIC, represented a new predicted behavior, which we termed “balance detection,” because it shows a maximal response when both ligands are present at a specific ratio. All other functions, including the additive interaction at RLS = 1, LIC = 0 (Figure 4C, top middle), interpolated between these three archetypal functions (Figure S4E) (Hart et al., 2015; Tendler et al., 2015). The archetypal functions identified here differ from standard Boolean logic, since they depend asymptotically on ligand ratios, rather than absolute concentrations (**STAR Methods**). These conclusions remain qualitatively similar if one considers a finite extracellular volume (**STAR Methods**; Figures S5A and S5B). This analysis provides an intuitive way to understand the distribution of response profiles.

To better characterize the distribution of response profiles, we quantified the percentage of occurrences of each response type in regions around each of the archetypal responses (Figures S5C and S5D). All archetypal behaviors occurred, regardless of whether parameters were chosen from a full range of values or restricted to a biologically relevant range (**STAR Methods**). However, parameters in the biological range showed enrichment for the additive, balance detection, and imbalance detection response profiles (Figure S5E). We further note that natural biological parameters could have been selected by evolution for functionality, including the ability to generate balance or imbalance detection. Together, these results show that this minimal model can generate the full range of observed response profiles for biologically reasonable parameter values.

Complex Response Profiles Emerge from the Interplay of Receptor-Ligand Affinities and Activities

We next asked how the archetypal ligand integration modes arise within the model. To do so, we analyzed the corresponding parameter regimes in more detail (Figure S6). As expected, additive responses occur when the two ligands are approximately equivalent, forming signaling complexes with similar phosphorylation activities ($\epsilon_{1k} \sim \epsilon_{2k}$; Figures 5A and S6A). By contrast, ratiometric behaviors occur when signaling complexes containing one ligand have higher activities than those containing the other ($\epsilon_{1k} \ll \epsilon_{2k}$), such that a weaker ligand competitively inhibits activation by the other, stronger ligand (Figures 5B and S6B). Imbalance detection occurs when each receptor preferentially binds to a distinct ligand with which it forms a less active signaling complex (Figures 5C and S6C). When only one type of ligand is present, it can bind both receptors, forming signaling

complexes with both higher and lower activity. When both ligands are present, the affinity preferences cause ligands and receptors to self-sort and predominantly form less active signaling complexes, reducing total pathway activity (Figure 5E). Finally, balance detection occurs through a similar mechanism, except that the relative affinities are reversed, favoring formation of more active signaling complexes when both ligands are present (Figures 5D and S6D).

A critical feature of the model is that the overall activity of the pathway depends not only on how much of each ligand is complexed with receptors but also on how that ligand is distributed across the range of distinct possible receptor complexes. In the model, simply changing the activities of the complexes can result in completely different response profiles (Figures S4F and S4G). As a result, addition of a second ligand can change not only the amount of the first ligand that is bound to receptors but also, more importantly, the distribution of that ligand across different potential signaling complexes with distinct activities. This could explain how two ligands can exhibit similar receptor preferences but still combine in qualitatively different ways with a third ligand.

Taken together, these results indicate that promiscuous receptor-ligand binding interactions are sufficient to produce a diverse repertoire of specific multi-ligand response profiles, including those observed experimentally. They reveal how the full functional repertoire can be understood as interpolating among three archetypal functions (ratiometric, imbalance detection, and the predicted balance detection function). Finally, they show how these functions arise through specific relations between the affinity parameters that control what receptor complexes will form and the activity parameters that control how the resulting signaling complexes contribute to the cellular response. Thus, as suggested experimentally, the full spectrum of observed computations requires only the ability of receptors and ligands to compete to form a variety of distinct signaling complexes, and differences in the relative activities of those complexes. Despite its simplicity, this system allows for remarkable computational diversity.

Receptor Expression Reprograms Ligand Response Profiles

Within an organism, different cell types generally express receptors at different levels. Changes in receptor expression could in principle alter BMP responses in similar, or different, ways compared to changes in ligand concentrations. To gain insight into the possible role of receptor expression in pathway computations, we varied receptor expression levels in the model while holding the biochemical parameter values ($K_{ij}^D, K_{ijk}^T, \epsilon_{ijk}$) fixed. We repeated this analysis for different biochemical parameter sets. In these simulations, some biochemical parameter sets produced only a limited range of ligand integration modes (Figure 6A, left), while others were more versatile, capable of generating a diverse range of computations as receptor expression levels were varied (Figure 6A, right). The existence of such versatile parameter sets in the model suggests the hypothesis that different cell types, by expressing different receptor profiles, might compute different responses to the same ligands.

If the BMP pathway exhibits and utilizes such versatility, cell lines with different receptor expression profiles could show

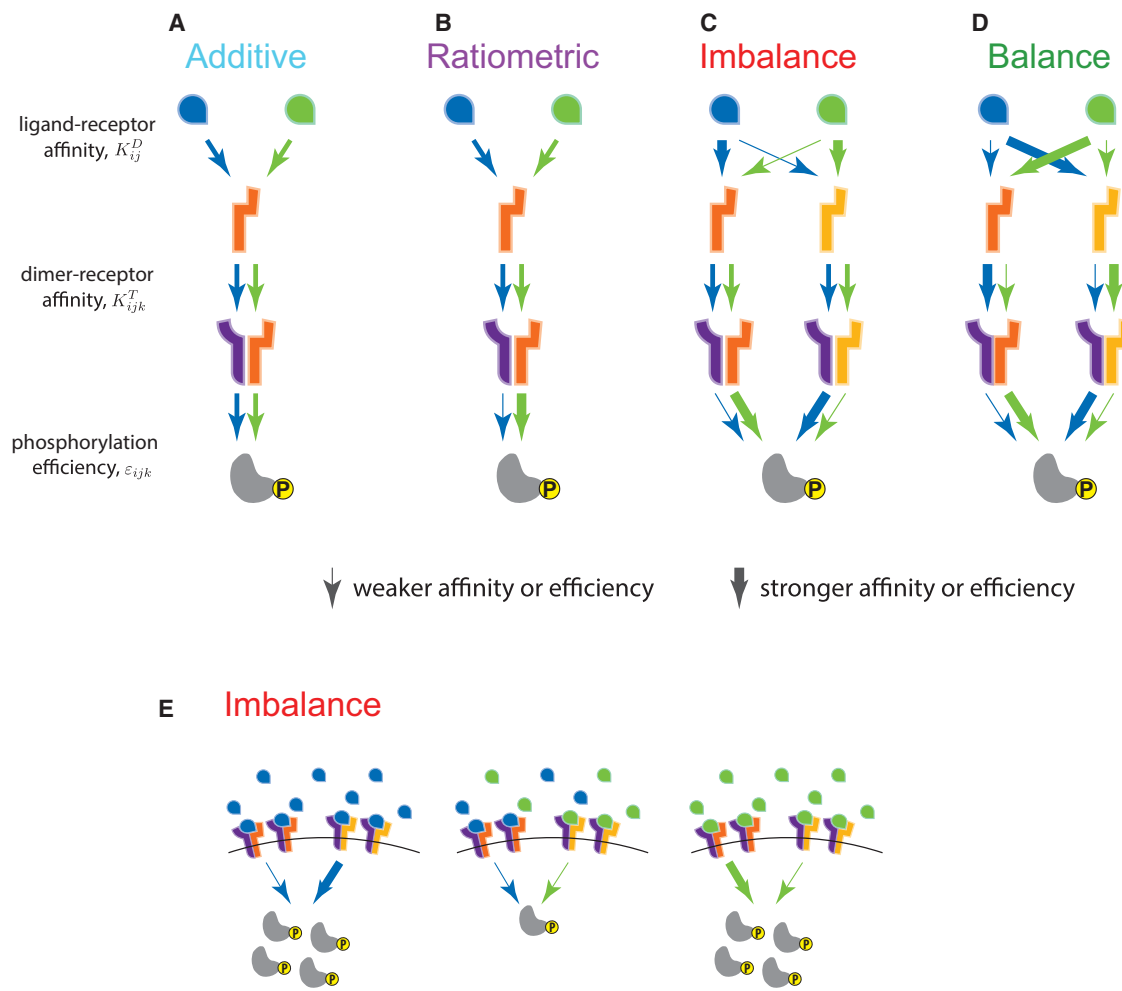


Figure 5. The Four Computational Archetypes Arise through the Interplay between Interaction Affinities and Complex Activity

Representative parameter regimes producing each of the four archetypes are indicated schematically. Upper and middle arrow thicknesses indicate the affinities K_{ij}^D and K_{ijk}^T , respectively. Lower arrow thicknesses indicate the phosphorylation rate of each signaling complex ε_{ijk} .

(A) When two ligands are equivalent (similar arrow thicknesses), they combine additively.

(B) When different ligands generate different levels of activity in complex with the same receptors (thin versus thick bottom arrows), the less active ligand (blue) competitively inhibits the more active ligand (green), leading to ratiometric behavior.

(C and D) Imbalance and balance detection regimes occur when affinity and activity parameters enable ligands to preferentially form less active (C) or more active (D) complexes, respectively.

(E) For example, in the parameter regime corresponding to the imbalance detection, cells exposed only to a single ligand species (i.e., only blue or green ligands) produce a mixture of strong and weakly active complexes (left, right), but cells exposed to mixtures of the two ligands predominantly form weakly active complexes (middle), leading to the imbalance detection behavior.

See also Figure S6.

distinct response profiles for the same ligands. To test this hypothesis, we compared the response of NMuMG cells to E14 mouse embryonic stem (ES) cells, which express less BMPR2 and ACVR1 and more ACVR2B (Figure 6B). As a control, we also analyzed NIH 3T3 fibroblasts, which had similar receptor expression to NMuMG cells (Figure 6B). The ES cells indeed exhibited different response profiles than NMuMG for the same ligands (Figures 6C–6E and S7A). Most strikingly, BMP4 and BMP9 integrated in an additive fashion in NMuMG and NIH 3T3 but showed the balance detection archetype in ES cells (Figure 6C). Other ligand pairs were also integrated similarly in NIH

3T3 and NMuMG but differently in ES cells (Figures 6D and 6E). Together, these results show that cell lines differ qualitatively in their ligand integration modes and in a manner that correlates with their receptor expression profiles, as predicted by the model. Furthermore, these results also validate the model prediction of balance detection (Figure 4G).

Reprogramming Response Profiles by Direct Manipulation of Receptor Expression Levels

Finally, to test whether changes in receptor expression are sufficient to reprogram computations, we directly perturbed receptor

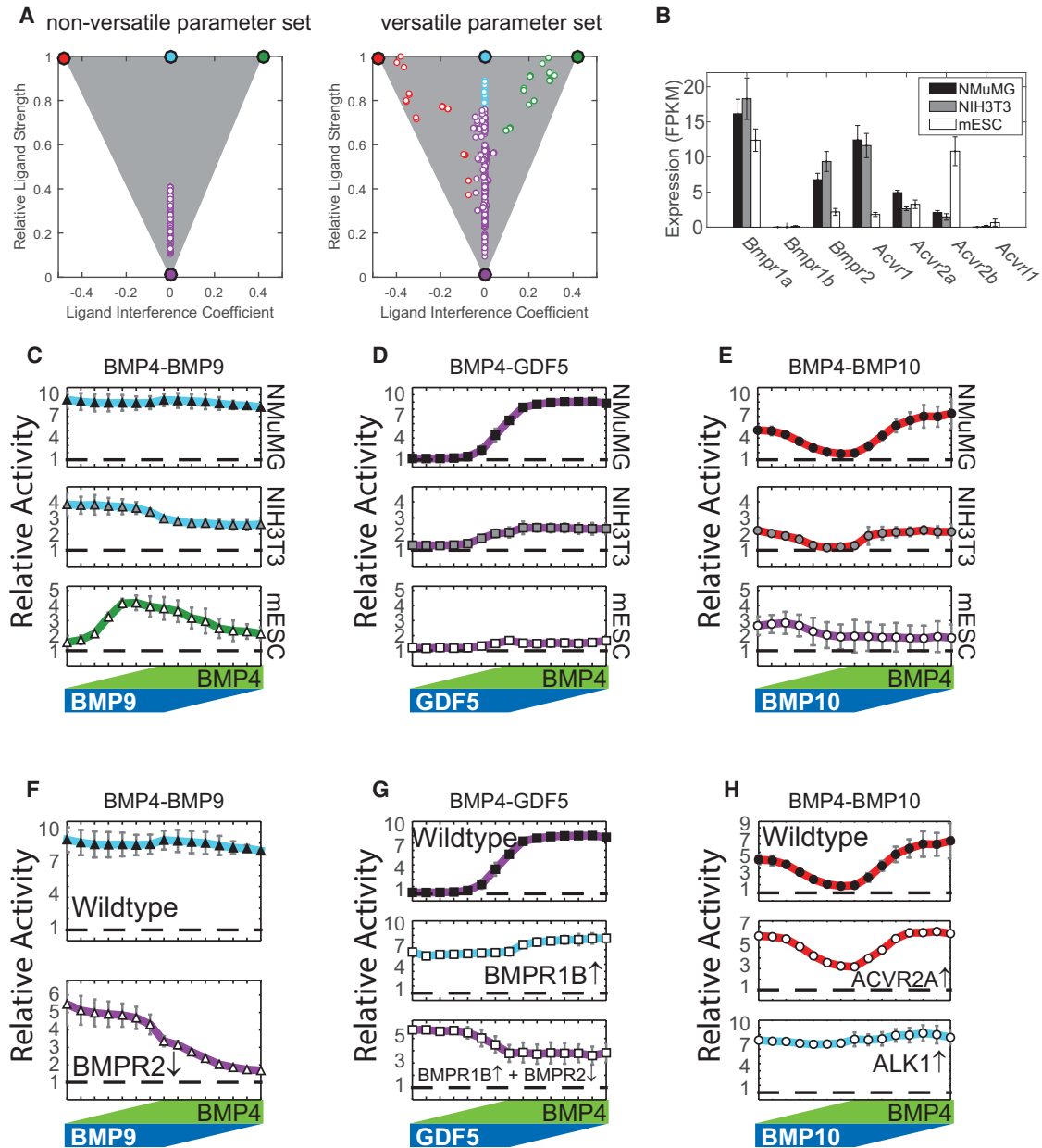


Figure 6. Receptor Expression Controls Computations

(A) Comparison of two simulated biochemical parameter sets (see Table S5 and STAR Methods for parameter values). For each set, multiple receptor expression profiles are plotted (individual dots). Dot color indicates the most similar archetype (cf. Figure 4C). For one parameter set (non-versatile, left), receptor expression only weakly affected computation. For the other parameter set (versatile, right), variation in receptor expression generates the full range of possible computations.

(B) BMP receptor expression profiles for three cell lines. Bars indicate expression levels of each receptor (fragments per kilobase of transcript per million mapped reads [FPKM]). Error bars represent SD of three independent biological replicates.

(C–E) Computation correlates with receptor expression pattern for three ligand pairs: BMP4-BMP9 (C), BMP4-GDF5 (D), and BMP4-BMP10 (E). Each column shows the response to the indicated pair of ligands for each cell line. Note the qualitative change in function between mouse embryonic stem cells (mESCs; bottom) and the other cell lines. Line colors refer to the closest archetype (cf. Figure 4C).

(F–H) Perturbing receptor expression level reprograms computations in NMuMG cells for the three ligand pairs: BMP4-BMP9 (F), BMP4-GDF5 (G), and BMP4-BMP10 (H). Wild-type cells (black points) were compared to cells with perturbed receptor expression (white points). Specific receptor perturbations are indicated next to each line, with up and down arrows indicating overexpression and siRNA, respectively.

In (C)–(H), error bars indicate SD of at least 3 replicates.

See also Figure S7 and Tables S3–S5.

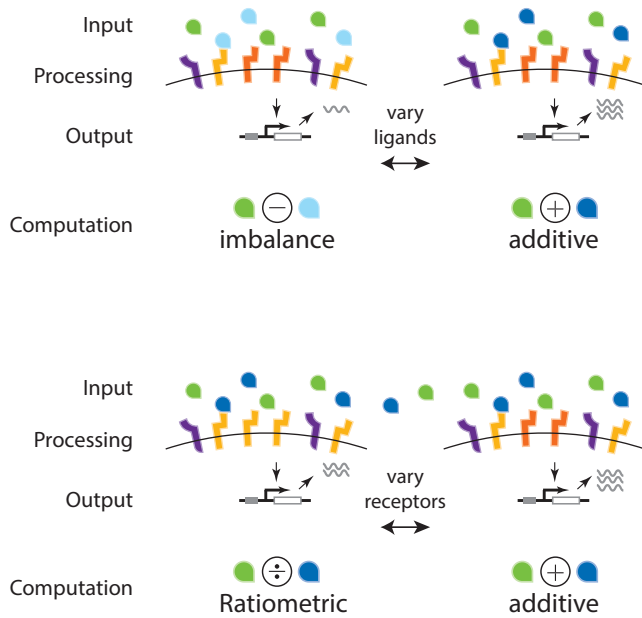


Figure 7. Schematic Illustration of Computational Plasticity in the BMP Signaling System

Ligand combinations represent inputs to the pathway, which processes them through receptor-ligand interactions to control the expression level of downstream target genes. In this scheme, a given receptor configuration can perform different computations on different ligand combinations (e.g., additive and imbalance, top), whereas cells expressing different receptor profiles can perform distinct computations on the same combination of ligands (e.g., ratiometric and additive, bottom).

expression in NMuMG cells. Depletion of the most highly expressed type II receptor in this cell type, BMPR2, with small interfering RNA (siRNA) changed the BMP4-BMP9 response from additive to ratiometric (Figures 6F and S7C). This indicates that BMP4 activates the pathway predominantly through BMPR2. By contrast, BMP9 can activate through other type II receptors, but BMP4 can effectively inhibit such BMPR2-independent BMP9 signaling.

As a second example, ectopically expressed BMPR1B, which is known to mediate GDF5 signaling (Nishitoh et al., 1996), enabled GDF5 to activate, rather than inhibit, the pathway, and thereby reprogrammed the ratiometric BMP4-GDF5 interaction to an additive one (Figures 6G and S7C). Furthermore, combining ectopic BMPR1B to enable GDF5 signaling with depletion of BMPR2 to reduce BMP4-dependent signaling inverted the ratiometric response (Figures 6G and S7C).

Third, we asked whether we could reprogram imbalance detection between BMP4 and BMP10 (Figure 2E). In the model, imbalance detection results from ligand competition for receptors. To alleviate this competition, we ectopically expressed the ALK1 receptor, which is known to mediate BMP9 and BMP10 signaling (David et al., 2007). This perturbation indeed removed competition, generating the predicted additive response (Figures 6H and S7C).

Taken together, these results show that receptor expression levels directly control computations and demonstrate that this effect enables rational manipulation of ligand integration modes using insights from the model (Figure S7B).

DISCUSSION

Our results show that promiscuous BMP receptor-ligand interactions enable cells to perceive information encoded in combinations of ligands (Figure 7). They do so through a specific set of computations over the multi-dimensional space of ligand concentrations, with the computations performed on a given set of ligands depending on the repertoire of receptors the cell expresses. These computations interpolate between archetypes loosely analogous to addition (additive, Figure 4D), subtraction (imbalance detection, Figure 4F), multiplication (balance detection, Figure 4G), and division (ratiometric, Figure 4E). This indicates that cells do not, in general, perceive ligand abundance but rather perceive specific functions of ligand combinations.

This system provides several key capabilities for cells. First, it is sensitive to both absolute concentrations of individual ligands and their relative concentrations. Encoding signals in relative ligand concentrations can increase robustness to variations in ligand accessibility, cell surface area, and other properties that affect all ligands in a correlated way. Second, computation is integrated with sensing. The system performs computations on ligand concentrations directly through competitive binding interactions, at steady state, without requiring regulatory cascades or transcriptional feedback loops. The observed computations arise because affinities among components need not correlate with the activities of the resulting signaling complexes. This allows ligands to compete for receptors to form a variety of distinct signaling complexes with distinct efficiencies. Third, and most intriguingly, this system possesses computational plasticity. By controlling the abundance of different receptor variants, a cell can control which computations it performs, and thus what features of the ligand environment it responds to. These capabilities could enable non-intuitive operative modes. For example, the use of ligand combinations may offer the ability to selectively activate a given cell type, since different cell types may respond to specific ligand combinations. Temporal changes in the concentration of a single ligand could elicit different, or opposite, changes in signal perception in distinct cell types.

These results should improve our ability to understand and manipulate natural BMP-dependent processes. For example, efficient primordial germ cell differentiation was shown to require a combination of both BMP4 and BMP8B homodimers, provoking the question of whether these ligands are integrated through balance detection (Ying et al., 2001). Conversely, BMP2 and BMP7 show opposing effects on ureter branching in developing kidneys (Piscione et al., 1997), suggesting they may operate in a ratiometric mode, and similar interactions were recently reported for BMP2 and GDF5 in multiple contexts (Klammert et al., 2015; Liu et al., 2016). The framework described here can be used to analyze these and other specific biological processes that utilize multiple BMPs (Açil et al., 2014; Bandyopadhyay et al., 2006; Chen et al., 2013). In the context of disease, many therapeutic strategies have focused on using a single ligand to treat conditions such as bone injuries and abnormalities, arthritis, diabetes, vascular conditions, obesity, and cancer (Kim and Choe, 2011; Wang et al.,

2003). Similarly, directed differentiation approaches in regenerative medicine often rely on a single BMP ligand. However, ligand combinations may provide more potent, and specific, control in these contexts.

Further work on higher dimensional combinations of ligands, as well as investigation of the effects of diffusible inhibitors such as Noggin and Chordin, will help to provide an understanding of systems like kidney development that depend on many different ligands, receptors, and modulators expressed in spatially and temporally overlapping patterns (Simic and Vukicevic, 2005). Similarly, quantitative analysis of receptor expression states will help elucidate the specific combination of ligands that each cell type senses. Experimental measurements of the effective parameter values for each specific molecular component in the BMP pathway could enable a more direct, quantitative, and predictive modeling framework. At a finer level, within a single cell type or state, fluctuations, or “noise,” in receptor expression could affect how cells perceive ligand combinations. However, within the model, typical levels of receptor expression noise show only mild effects (Figures S7D–S7H; STAR Methods).

Finally, further analysis could reveal additional computations beyond those described above. Extending the model to include the TGF- β ligands could be used to understand newly discovered ligand-level competition between the two branches of this signaling pathway (Hatsell et al., 2015; Lowery et al., 2015; Olsen et al., 2015) and incorporate them into a single framework. More generally, Wnt, FGF, JAK-STAT, Eph-Ephrin, and other signaling pathways also exhibit promiscuous interactions between multiple ligand, receptor, and co-receptor variants and may function according to similar principles (Jørgensen et al., 2009; Murray, 2007; Wodarz and Nusse, 1998). Future elucidation of the principles of programmable computation through promiscuous receptor-ligand interactions could be used to engineer precise multicellular behaviors for synthetic biology and tissue engineering applications.

STAR★METHODS

Detailed methods are provided in the online version of this paper and include the following:

- KEY RESOURCES TABLE
- CONTACT FOR REAGENT AND RESOURCE SHARING
- EXPERIMENTAL MODEL AND SUBJECT DETAILS
 - Tissue culture and cell lines
 - Sensor cell lines construction
- METHOD DETAILS
 - BMP response and flow cytometry
 - Ligand integration survey
 - SDS-PAGE and immunoblotting
 - BMP response with heparinase I/III
 - BMP response with NaClO₃
 - Receptor overexpression
 - siRNA induced knock-down
 - Quantitative PCR
 - Antibody detection for phospho-SMAD1/5/8
 - Time-lapse imaging

- Mathematical model for promiscuous interactions
- Solving the steady-state equations
- The error function and least square minimization
- Dimensional reduction
- The (2,2,2) model and parameter selection
- Phenotypical parameters
- The four archetypes and the structure of parameter space
- Computations depend only on ligand ratios at high ligand concentrations
- Archetypal computations differ from Boolean logic gates
- Biological parameter range
- Versatility search
- Robustness to perturbations in receptor expression
- Finite volume of extracellular space
- Signaling modifiers
- Nonlinear signal accumulation
- Additional features of the BMP pathway
- Spatial heterogeneity

● QUANTIFICATION AND STATISTICAL ANALYSIS

- Average and variability analysis
- Assignment of integration modes in survey
- RNaseq Analyses

● DATA AND SOFTWARE AVAILABILITY

SUPPLEMENTAL INFORMATION

Supplemental Information includes seven figures and five tables and can be found with this article online at <http://dx.doi.org/10.1016/j.cell.2017.08.015>.

AUTHOR CONTRIBUTIONS

Y.E.A., J.M.L., and M.B.E. conceived and designed the experiments. Y.E.A., J.M.L., H.K., M.G., and R.M. performed the experiments. Y.E.A., J.M.L., H.K., and M.G. analyzed the experimental data. Y.E.A., B.B., and C.S. developed the mathematical models. Y.E.A., J.M.L., and M.B.E. wrote the paper.

ACKNOWLEDGMENTS

We thank Uri Alon, James Briscoe, Marcelo Ehrlich, Jordi Garcia-Ojalvo, Lea Goentoro, Roy Kishony, Vicki Rosen, Boris Shraiman, Ned Wingreen, and members of the Elowitz lab for helpful discussions and feedback. We thank the Caltech Flow Cytometry Facility and the Millard and Muriel Jacobs Genetics and Genomics Laboratory at Caltech for technical assistance. This work was supported by the Gordon and Betty Moore Foundation (grant GBMF2809 to the Caltech Programmable Molecular Technology Initiative), the Human Frontiers Science Program (grant RGP0020), the NIH (grant R01 HD75335A), the Defense Advanced Research Projects Agency (contract HR0011-16-0138), and the Institute for Collaborative Biotechnologies (grant W911NF-09-0001 from the US Army Research Office). This work does not necessarily reflect the position or policy of the US Government, and no official endorsement should be inferred. H.K. is supported by a National Science Foundation graduate research fellowship (grant DGE-1144469). C.S. is supported by the NIH (National Institute of General Medical Sciences training grant T32 GM008042) and by a David Geffen Medical Scholarship. Y.E.A., J.M.L., and M.B.E. filed a provisional patent application relating to this work.

Received: October 4, 2016

Revised: April 26, 2017

Accepted: August 8, 2017

Published: September 7, 2017

REFERENCES

- Açıl, Y., Ghoniem, A.-A., Wiltfang, J., and Gierloff, M. (2014). Optimizing the osteogenic differentiation of human mesenchymal stromal cells by the synergistic action of growth factors. *J. Craniomaxillofac. Surg.* 42, 2002–2009.
- Afgan, E., Baker, D., van den Beek, M., Blankenberg, D., Bouvier, D., Čech, M., Chilton, J., Clements, D., Coraor, N., Eberhard, C., et al. (2016). The Galaxy platform for accessible, reproducible and collaborative biomedical analyses: 2016 update. *Nucleic Acids Res.* 44 (W1), W3–W10.
- Afrakhte, M., Morén, A., Jossan, S., Itoh, S., Sampath, K., Westermark, B., Hedin, C.-H., Hedin, N.-E., and ten Dijke, P. (1998). Induction of inhibitory Smad6 and Smad7 mRNA by TGF- β family members. *Biochem. Biophys. Res. Commun.* 249, 505–511.
- Atkinson, D.E. (1968). The energy charge of the adenylate pool as a regulatory parameter. Interaction with feedback modifiers. *Biochemistry* 7, 4030–4034.
- Aykul, S., and Martinez-Hackert, E. (2016). Transforming growth factor- β family ligands can function as antagonists by competing for type II receptor binding. *J Biol Chem.* 291, 10792–10804.
- Balemans, W., and Van Hul, W. (2002). Extracellular regulation of BMP signaling in vertebrates: a cocktail of modulators. *Dev. Biol.* 250, 231–250.
- Bandyopadhyay, A., Tsuji, K., Cox, K., Harfe, B.D., Rosen, V., and Tabin, C.J. (2006). Genetic analysis of the roles of BMP2, BMP4, and BMP7 in limb patterning and skeletogenesis. *PLoS Genet.* 2, e216.
- Berg, J., Hung, Y.P., and Yellen, G. (2009). A genetically encoded fluorescent reporter of ATP:ADP ratio. *Nat. Methods* 6, 161–166.
- Cheifetz, S. (1999). BMP receptors in limb and tooth formation. *Crit. Rev. Oral Biol. Med.* 10, 182–198.
- Chen, H., Brady Ridgway, J., Sai, T., Lai, J., Warming, S., Chen, H., Roose-Girma, M., Zhang, G., Shou, W., and Yan, M. (2013). Context-dependent signaling defines roles of BMP9 and BMP10 in embryonic and postnatal development. *Proc. Natl. Acad. Sci. USA* 110, 11887–11892.
- Danesh, S.M., Villasenor, A., Chong, D., Soukup, C., and Cleaver, O. (2009). BMP and BMP receptor expression during murine organogenesis. *Gene Expr. Patterns* 9, 255–265.
- David, L., Mallet, C., Mazerbourg, S., Feige, J.-J., and Baily, S. (2007). Identification of BMP9 and BMP10 as functional activators of the orphan activin receptor-like kinase 1 (ALK1) in endothelial cells. *Blood* 109, 1953–1961.
- David, L., Mallet, C., Keramidas, M., Lamandé, N., Gasc, J.-M., Dupuis-Girod, S., Plauchu, H., Feige, J.-J., and Baily, S. (2008). Bone morphogenetic protein-9 is a circulating vascular quiescence factor. *Circ. Res.* 102, 914–922.
- Delos Santos, R.C., Garay, C., and Antonescu, C.N. (2015). Charming neighborhoods on the cell surface: plasma membrane microdomains regulate receptor tyrosine kinase signaling. *Cell. Signal.* 27, 1963–1976.
- Ding, S., Wu, X., Li, G., Han, M., Zhuang, Y., and Xu, T. (2005). Efficient transposition of the piggyBac (PB) transposon in mammalian cells and mice. *Cell* 122, 473–483.
- Dudley, A.T., and Robertson, E.J. (1997). Overlapping expression domains of bone morphogenetic protein family members potentially account for limited tissue defects in BMP7 deficient embryos. *Dev. Dyn.* 208, 349–362.
- Edson, M.A., Nalam, R.L., Clementi, C., Franco, H.L., Demayo, F.J., Lyons, K.M., Pangas, S.A., and Matzuk, M.M. (2010). Granulosa cell-expressed BMPR1A and BMPR1B have unique functions in regulating fertility but act redundantly to suppress ovarian tumor development. *Mol. Endocrinol.* 24, 1251–1266.
- Elowitz, M.B., Levine, A.J., Siggia, E.D., and Swain, P.S. (2002). Stochastic gene expression in a single cell. *Science* 297, 1183–1186.
- Escalante-Chong, R., Savir, Y., Carroll, S.M., Ingraham, J.B., Wang, J., Marx, C.J., and Springer, M. (2015). Galactose metabolic genes in yeast respond to a ratio of galactose and glucose. *Proc. Natl. Acad. Sci. USA* 112, 1636–1641.
- Faber, S.C., Robinson, M.L., Makarenko, H.P., and Lang, R.A. (2002). Bmp signaling is required for development of primary lens fiber cells. *Development* 129, 3727–3737.
- Gibson, D.G., Young, L., Chuang, R.-Y., Venter, J.C., Hutchison, C.A., 3rd, and Smith, H.O. (2009). Enzymatic assembly of DNA molecules up to several hundred kilobases. *Nat. Methods* 6, 343–345.
- Gilboa, L., Nohe, A., Geissendorfer, T., Sebald, W., Henis, Y.I., and Knaus, P. (2000). Bone morphogenetic protein receptor complexes on the surface of live cells: a new oligomerization mode for serine/threonine kinase receptors. *Mol. Biol. Cell* 11, 1023–1035.
- Hart, Y., Sheftel, H., Haussler, J., Szekely, P., Ben-Moshe, N.B., Korem, Y., Tendler, A., Mayo, A.E., and Alon, U. (2015). Inferring biological tasks using Pareto analysis of high-dimensional data. *Nat. Methods* 12, 233–235.
- Hatsell, S.J., Idone, V., Wolken, D.M.A., Huang, L., Kim, H.J., Wang, L., Wen, X., Nannuru, K.C., Jimenez, J., Xie, L., et al. (2015). ACVR1R206H receptor mutation causes fibrodysplasia ossificans progressiva by imparting responsiveness to activin A. *Sci. Transl. Med.* 7, 303ra137.
- Heggebo, J., Haasters, F., Polzer, H., Schwarz, C., Saller, M.M., Mutschler, W., Schieker, M., and Prall, W.C. (2014). Aged human mesenchymal stem cells: the duration of bone morphogenetic protein-2 stimulation determines induction or inhibition of osteogenic differentiation. *Orthop. Rev. (Pavia)* 6, 5242.
- Heinecke, K., Seher, A., Schmitz, W., Mueller, T.D., Sebald, W., and Nickel, J. (2009). Receptor oligomerization and beyond: a case study in bone morphogenetic proteins. *BMC Biol.* 7, 59.
- Hedin, C.H., Miyazono, K., and ten Dijke, P. (1997). TGF-beta signalling from cell membrane to nucleus through SMAD proteins. *Nature* 390, 465–471.
- Inman, G.J., Nicolás, F.J., and Hill, C.S. (2002). Nucleocytoplasmic shuttling of Smads 2, 3, and 4 permits sensing of TGF-beta receptor activity. *Mol. Cell* 10, 283–294.
- Israel, D.I., Nove, J., Kerns, K.M., Kaufman, R.J., Rosen, V., Cox, K.A., and Wozney, J.M. (1996). Heterodimeric bone morphogenetic proteins show enhanced activity in vitro and in vivo. *Growth Factors* 13, 291–300.
- Jørgensen, C., Sherman, A., Chen, G.I., Pascalescu, A., Poliakov, A., Hsiung, M., Larsen, B., Wilkinson, D.G., Linding, R., and Pawson, T. (2009). Cell-specific information processing in segregating populations of Eph receptor ephrin-expressing cells. *Science* 326, 1502–1509.
- Kim, M., and Choe, S. (2011). BMPs and their clinical potentials. *BMB Rep.* 44, 619–634.
- Klammert, U., Mueller, T.D., Hellmann, T.V., Wuerzler, K.K., Kotzsch, A., Schliermann, A., Schmitz, W., Kuebler, A.C., Sebald, W., and Nickel, J. (2015). GDF-5 can act as a context-dependent BMP-2 antagonist. *BMC Biol.* 13, 77.
- Korchynskyi, O., and ten Dijke, P. (2002). Identification and functional characterization of distinct critically important bone morphogenetic protein-specific response elements in the Id1 promoter. *J. Biol. Chem.* 277, 4883–4891.
- Lavery, K., Swain, P., Falb, D., and Alaoui-Ismaili, M.H. (2008). BMP-2/4 and BMP-6/7 differentially utilize cell surface receptors to induce osteoblastic differentiation of human bone marrow-derived mesenchymal stem cells. *J. Biol. Chem.* 283, 20948–20958.
- Li, X., Ionescu, A.M., Schwarz, E.M., Zhang, X., Drissi, H., Puzas, J.E., Rosier, R.N., Zuscik, M.J., and O'Keefe, R.J. (2003). Smad6 is induced by BMP-2 and modulates chondrocyte differentiation. *J. Orthop. Res.* 21, 908–913.
- Liu, J., Saito, K., Maruya, Y., Nakamura, T., Yamada, A., Fukumoto, E., Ishikawa, M., Iwamoto, T., Miyazaki, K., Yoshizaki, K., et al. (2016). Mutant GDF5 enhances ameloblast differentiation via accelerated BMP2-induced Smad1/5/8 phosphorylation. *Sci. Rep.* 6, 23670.
- Llimargas, M., and Lawrence, P.A. (2001). Seven Wnt homologues in Drosophila: a case study of the developing tracheae. *Proc. Natl. Acad. Sci. USA* 98, 14487–14492.
- Long, L., Ormiston, M.L., Yang, X., Southwood, M., Gräf, S., Machado, R.D., Mueller, M., Kinzel, B., Yung, L.M., Wilkinson, J.M., et al. (2015). Selective enhancement of endothelial BMPR-II with BMP9 reverses pulmonary arterial hypertension. *Nat. Med.* 21, 777–785.
- Lorda-Diez, C.I., Montero, J.A., and Choe, S. (2014). Ligand-and stage-dependent divergent functions of bmp signaling in the differentiation of embryonic skeletogenic progenitors in vitro. *J. Bone Miner. Res.* 29, 735–748.

- Lowery, J.W., Intini, G., Gamer, L., Lotinun, S., Salazar, V.S., Ote, S., Cox, K., Baron, R., and Rosen, V. (2015). Loss of BMPR2 leads to high bone mass due to increased osteoblast activity. *J. Cell Sci.* 128, 1308–1315.
- Madl, J.E., and Herman, R.K. (1979). Polyploids and sex determination in *Cae-norhabditis elegans*. *Genetics* 93, 393–402.
- Massagué, J. (1998). TGF-beta signal transduction. *Annu. Rev. Biochem.* 67, 753–791.
- Mueller, T.D., and Nickel, J. (2012). Promiscuity and specificity in BMP receptor activation. *FEBS Lett.* 586, 1846–1859.
- Murray, P.J. (2007). The JAK-STAT signaling pathway: input and output integration. *J. Immunol.* 178, 2623–2629.
- Neugebauer, J.M., Kwon, S., Kim, H.-S., Donley, N., Tilak, A., Sopory, S., and Christian, J.L. (2015). The prodomain of BMP4 is necessary and sufficient to generate stable BMP4/7 heterodimers with enhanced bioactivity in vivo. *Proc. Natl. Acad. Sci. USA* 112, E2307–E2316.
- Nickel, J., Sebald, W., Groppe, J.C., and Mueller, T.D. (2009). Intricacies of BMP receptor assembly. *Cytokine Growth Factor Rev.* 20, 367–377.
- Nicklas, D., and Saiz, L. (2013). Computational modelling of Smad-mediated negative feedback and crosstalk in the TGF- β superfamily network. *J R Soc Interface* 10, 20130363.
- Nishitoh, H., Ichijo, H., Kimura, M., Matsumoto, T., Makishima, F., Yamaguchi, A., Yamashita, H., Enomoto, S., and Miyazono, K. (1996). Identification of type I and type II serine/threonine kinase receptors for growth/differentiation factor-5. *J. Biol. Chem.* 271, 21345–21352.
- Nohe, A., Keating, E., Knaus, P., and Petersen, N.O. (2004). Signal transduction of bone morphogenetic protein receptors. *Cell. Signal.* 16, 291–299.
- Olsen, O.E., Wader, K.F., Hella, H., Mylin, A.K., Turesson, I., Nesthus, I., Wagle, A., Sundan, A., and Holien, T. (2015). Activin A inhibits BMP-signaling by binding ACVR2A and ACVR2B. *Cell Commun. Signal.* 13, 27.
- Piek, E., Moustakas, A., Kurisaki, A., Heldin, C.H., and ten Dijke, P. (1999). TGF-(beta) type I receptor/ALK-5 and Smad proteins mediate epithelial to mesenchymal transdifferentiation in NMuMG breast epithelial cells. *J. Cell Sci.* 112, 4557–4568.
- Piscione, T.D., Yager, T.D., Gupta, I.R., Grinfeld, B., Pei, Y., Attisano, L., Wrana, J.L., and Rosenblum, N.D. (1997). BMP-2 and OP-1 exert direct and opposite effects on renal branching morphogenesis. *Am. J. Physiol.* 273, F961–F975.
- Ricard, N., Caiats, D., Levet, S., Subileau, M., Mallet, C., Zimmers, T.A., Lee, S.-J., Bidart, M., Feige, J.-J., and Baily, S. (2012). BMP9 and BMP10 are critical for postnatal retinal vascular remodeling. *Blood* 119, 6162–6171.
- Rosenzweig, B.L., Imamura, T., Okadome, T., Cox, G.N., Yamashita, H., ten Dijke, P., Heldin, C.H., and Miyazono, K. (1995). Cloning and characterization of a human type II receptor for bone morphogenetic proteins. *Proc. Natl. Acad. Sci. USA* 92, 7632–7636.
- Salazar, V.S., Gamer, L.W., and Rosen, V. (2016). BMP signalling in skeletal development, disease and repair. *Nat. Rev. Endocrinol.* 12, 203–221.
- Schmierer, B., and Hill, C.S. (2007). TGFbeta-SMAD signal transduction: molecular specificity and functional flexibility. *Nat. Rev. Mol. Cell Biol.* 8, 970–982.
- Simic, P., and Vukicevic, S. (2005). Bone morphogenetic proteins in development and homeostasis of kidney. *Cytokine Growth Factor Rev.* 16, 299–308.
- Smith, A.G. (2001). Embryo-derived stem cells: of mice and men. *Annu. Rev. Cell Dev. Biol.* 17, 435–462.
- Storm, E.E., and Kingsley, D.M. (1996). Joint patterning defects caused by single and double mutations in members of the bone morphogenetic protein (BMP) family. *Development* 122, 3969–3979.
- Szymczak, A.L., and Vignali, D.A. (2005). Development of 2A peptide-based strategies in the design of multicistronic vectors. *Expert Opin. Biol. Ther.* 5, 627–638.
- Tendler, A., Mayo, A., and Alon, U. (2015). Evolutionary tradeoffs, Pareto optimality and the morphology of ammonite shells. *BMC Syst. Biol.* 9, 12.
- Valera, E., Isaacs, M.J., Kawakami, Y., and Belmonte, J. (2010). BMP-2/6 heterodimer is more effective than BMP-2 or BMP-6 homodimers as inductor of differentiation of human embryonic stem cells. *PLoS One.* 5, e11167.
- Ventura, F., Doody, J., and Massague, J. (1995). Human type II receptor for bone morphogenetic proteins (BMPs): extension of the two-kinase receptor model to the BMPs. *Mol. Cell. Biol.* 15, 3479–3486.
- Vilar, J.M.G., Jansen, R., and Sander, C. (2006). Signal processing in the TGF-beta superfamily ligand-receptor network. *PLoS Comput. Biol.* 2, e3.
- Wakefield, L.M., Smith, D.M., Masui, T., Harris, C.C., and Sporn, M.B. (1987). Distribution and modulation of the cellular receptor for transforming growth factor-beta. *J. Cell Biol.* 105, 965–975.
- Wang, S., Chen, Q., Simon, T.C., and Strebeck, F. (2003). Bone morphogenetic protein-7 (BMP-7), a novel therapy for diabetic nephropathy1. *Kidney Int.* 63, 2037–2049.
- Warmflash, A., Zhang, Q., Sorre, B., Vonica, A., Siggia, E.D., and Brivanlou, A.H. (2012). Dynamics of TGF- β signaling reveal adaptive and pulsatile behaviors reflected in the nuclear localization of transcription factor Smad4. *Proc. Natl. Acad. Sci. USA* 109, E1947–E1956.
- Wodarz, A., and Nusse, R. (1998). Mechanisms of Wnt signaling in development. *Annu. Rev. Cell Dev. Biol.* 14, 59–88.
- Wu, S.C.-Y., Meir, Y.-J.J., Coates, C.J., Handler, A.M., Pelczar, P., Moisyadi, S., and Kaminski, J.M. (2006). piggyBac is a flexible and highly active transposon as compared to sleeping beauty, Tol2, and Mos1 in mammalian cells. *Proc. Natl. Acad. Sci. USA* 103, 15008–15013.
- Ying, Y., and Zhao, G.Q. (2001). Cooperation of endoderm-derived BMP2 and extraembryonic ectoderm-derived BMP4 in primordial germ cell generation in the mouse. *Dev. Biol.* 232, 484–492.
- Ying, Y., Liu, X.M., Marble, A., Lawson, K.A., and Zhao, G.Q. (2000). Requirement of Bmp8b for the generation of primordial germ cells in the mouse. *Mol. Endocrinol.* 14, 1053–1063.
- Ying, Y., Qi, X., and Zhao, G.Q. (2001). Induction of primordial germ cells from murine epiblasts by synergistic action of BMP4 and BMP8B signaling pathways. *Proc. Natl. Acad. Sci. USA* 98, 7858–7862.
- Zakin, L., and De Robertis, E.M. (2010). Extracellular regulation of BMP signaling. *Curr. Biol.* 20, R89–R92.
- Zi, Z., Chapnick, D.A., and Liu, X. (2012). Dynamics of TGF- β /Smad signaling. *FEBS Lett.* 586, 1921–1928.

STAR★METHODS

KEY RESOURCES TABLE

| REAGENT or RESOURCE | SOURCE | IDENTIFIER |
|--|--|-----------------------------|
| Antibodies | | |
| Rabbit monoclonal anti phospho-SMAD1/5/8 | Cell Signaling Technology | Cat#13820; RRID: AB_2493181 |
| Rabbit monoclonal anti phospho-p44/42 MAPK | Cell Signaling Technology | Cat#4370; RRID: AB_2315112 |
| Rabbit monoclonal anti SMAD1 | Cell Signaling Technology | Cat#6944; RRID: AB_10858882 |
| Rabbit polyclonal anti BMPR2 | Cell Signaling Technology | Cat#6979; RRID: AB_10889249 |
| Rabbit monoclonal anti GAPDH | Cell Signaling Technology | Cat#2118; RRID: AB_561053 |
| Goat anti-rabbit IgG | Cell Signaling Technology | Cat#7074; RRID: AB_2099233 |
| Bacterial and Virus Strains | | |
| Biological Samples | | |
| Chemicals, Peptides, and Recombinant Proteins | | |
| Recombinant BMP proteins (see Table S1) | R&D Systems | See Table S1 |
| Recombinant Murine BMP-4 | Peprotech | Cat#315-27 |
| Recombinant Human BMP-10 | Peprotech | Cat#120-40 |
| Recombinant Murine GDF-5 | Peprotech | Cat#315-24 |
| Fetal Bovine Serum | ThermoFisher | Cat#10439024 |
| Fetal Bovine Serum | Clontech | Cat#631106 |
| Cosmic Calf Serum | Hyclone | Cat#SH30087.03 |
| Leukemia Inhibiting Factor | ThermoFisher | Cat#ESG1107 |
| Heparinase I/III | Sigma | Cat#H3917 |
| Sodium Chlorate | Sigma | Cat#S3171 |
| 20X LumiGLO Reagent and 20X Peroxide | Cell Signaling Technology | Cat#7003 |
| Halt protease inhibitor | ThermoFisher | Cat#87785 |
| RNAiMAX | ThermoFisher | Cat#13778075 |
| Lipofectamine LTX | ThermoFisher | Cat#15338100 |
| Fugene HD | Promega | Cat#E2311 |
| Critical Commercial Assays | | |
| RNAeasy mini kit | QIAGEN | Cat#74104 |
| iScript cDNA synthesis kit | BioRad | Cat#1708890 |
| IQ SYBR Green Supermix | BioRad | Cat#1708882 |
| SsoAdvanced Universal probes Supermix | BioRad | Cat#1725281 |
| NEBNext Ultra RNA-seq kit | NEB | Cat#E7530 |
| Deposited Data | | |
| RNAseq data | This paper | GEO: GSE98674 |
| Experimental Models: Cell Lines | | |
| NMuMG | ATCC | CRL-1636 |
| NIH 3T3 | ATCC | CRL-1658 |
| E14 mouse ES cells (E14Tg2a.4) | Laboratory of Bill Skarnes and Peri Tate | N/A |
| NMuMG Sensor line | This paper | N/A |
| NIH 3T3 Sensor line | This paper | N/A |
| mESC Sensor line | This paper | N/A |

(Continued on next page)

Continued

| REAGENT or RESOURCE | SOURCE | IDENTIFIER |
|--|--------------------|---|
| Experimental Models: Organisms/Strains | | |
| Oligonucleotides | | |
| siRNA targeting BMP receptors (see Table S3) | This paper | See Table S3 |
| siRNA targeting BMP modulators (see Table S3) | This paper | See Table S3 |
| qPCR primers and probes (see Table S4) | This paper | N/A |
| qPCR primers (see Table S4) | This paper | N/A |
| Recombinant DNA | | |
| pcDNA5 BRE mCMV Citrine HygroR | This paper | N/A |
| Pb510b Bmpr1a T2A mTurquoise NeoR | This paper | N/A |
| Pb510b Bmpr1b T2A mTurquoise NeoR | This paper | N/A |
| Pb510b Bmpr2 T2A mTurquoise NeoR | This paper | N/A |
| Pb510b Acvr1 T2A mTurquoise NeoR | This paper | N/A |
| Pb510b Acvr2a T2A mTurquoise NeoR | This paper | N/A |
| Pb510b Acvr2b T2A mTurquoise NeoR | This paper | N/A |
| Pb510b Alk1 T2A mTurquoise NeoR | This paper | N/A |
| Software and Algorithms | | |
| MATLAB | MathWorks | N/A |
| MATLAB based flow cytometry analysis software | This paper | N/A |
| MATLAB code for simulating ligand-receptor interactions | This paper | N/A |
| Galaxy (RNAseq analysis) | Afgan et al., 2016 | https://usegalaxy.org/ |

CONTACT FOR REAGENT AND RESOURCE SHARING

Further information and requests for resources and reagents should be directed to and will be fulfilled by the Lead Contact, Michael B. Elowitz (melowitz@caltech.edu).

EXPERIMENTAL MODEL AND SUBJECT DETAILS**Tissue culture and cell lines**

NMuMG (NAMRU Mouse Mammary Gland cells, female) and NIH 3T3 (mouse fibroblast, male) cells were acquired from ATCC (CRL-1636 and CRL-1658, respectively). E14 cells (mouse embryonic stem cells, E14Tg2a.4, male) were obtained from Bill Skarnes and Peri Tate. All cells were cultured in a humidity controlled chamber at 37°C with 5% CO₂. NMuMG cells were cultured in DMEM supplemented with 10% FBS (Clonetech #631367), 1mM sodium pyruvate, 1unit/ml penicillin, 1µg/ml streptomycin, 2mM L-glutamine and 1X MEM non-essential amino acids. NIH 3T3 cells were cultured in DMEM supplemented with 10% CCS (Hyclone #SH30087), 1mM sodium pyruvate, 1unit/ml penicillin, 1µg/ml streptomycin and 2mM L-glutamine. ES cells were plated on tissue culture plates pre-coated with 0.1% gelatin and cultured in standard pluripotency-maintaining conditions (Smith, 2001) using DMEM supplemented with 15% FBS (ES qualified, GIBCO #16141), 1mM sodium pyruvate, 1unit/ml penicillin, 1µg/ml streptomycin, 2mM L-glutamine, 1X MEM non-essential amino acids, 55mM β-mercaptoethanol, and 1000Units/ml leukemia inhibitory factor (LIF).

Sensor cell lines construction

Construction of the reporter cell lines was carried out via random integration of a plasmid harboring the BMP response element (BRE) ([Korchynskyi and ten Dijke, 2002](#)) in the enhancer region of a minimal CMV driving the expression of an H2B-Citrine protein fusion. ES cells were transfected using the FugeneHD reagent. NMuMG and 3T3 cells were transfected using Lipofectamine LTX. After transfection, cells were selected with 100µg/ml hygromycin. All experiments were performed with clonal populations, generated via colony picking (ES) or limiting dilutions (NMuMG, NIH 3T3). To ensure results were not dependent on the specific reporter integration site, an independent BRE-reporter cell line was generated using PiggyBac integration (SBI) ([Figure S2C](#)).

METHOD DETAILS

BMP response and flow cytometry

Sensor cell lines were plated at 40% confluence in 96 well plates and cultured under standard conditions (above) for 12 hr. Media was then replaced and ligand(s) were added at specified concentrations. 24 hr after ligand addition, cells were prepared for flow cytometry in the following way: Cells were washed with PBS and lifted from the plate using either 0.05 mL Accutase (ES cells) or trypsin (NMuMG and 3T3 cells) for 5 min at 37°C. Protease activity was quenched by re-suspending the cells in HBSS with 2.5mg/ml Bovine Serum Albumin (BSA). Cells were then filtered with a 40 μ m mesh and analyzed by flow cytometry (MACSQuant VYB, Miltenyi). All recombinant BMP ligands were acquired from R&D Systems (Table S1), with the exception of Figure S2D where BMP4, BMP10 and GDF5 were acquired from Peprotech.

Ligand integration survey

In order to identify non-additive ligand integration modes, cells were exposed to a matrix of ligands at predetermined concentrations. We selected concentrations that were sufficient to induce responses in cells already known to respond to those ligands, but not so high as to induce potential non-specific responses. For this reason, we based ligand concentrations on supplier data, and selected a concentration at the high end of the input dynamic range for a cell based system susceptible to each ligand (see Table S1). All BMP ligands used in the survey were acquired from R&D Systems (see Table S1 for more information).

SDS-PAGE and immunoblotting

Phospho-SMAD1/5/8

For assessment of phospho-SMAD1/5/8, cells were plated at 40% confluence under standard conditions in 24 well plates. To reduce phospho-SMAD1/5/8 background activity, cells were transferred to reduced serum media containing 1.0% FBS for 12 hr. This media was then exchanged for DMEM and cells were incubated at 37°C for another 6 hr. DMEM was then replaced and ligands were added in DMEM at the specified concentrations and incubated at 37°C for 20 min. Cells were then treated with 50 μ l lysis buffer (Cell Signaling 9803) with the following additions: 0.1M DTT, 50mM NaF, 1mM PMSF and additional protease inhibitors (Thermo 87785). Samples were immediately stored at -80°C until processed for SDS-PAGE. SDS-PAGE was conducted using NuPAGE Bis-Tris Mini Gels 4%-12% (Thermo). Approximately 10-20 μ g of total protein, denatured by heat, was loaded per well. Samples were run at 50mA for approximately 60 min. Protein was transferred from gels to nitrocellulose using the iBlot apparatus and iBlot reagents (Thermo) applying program 2 for 8 min. Membranes were trimmed and blocked with 5% milk in Tris buffered saline with 0.1% Tween 20 (TBST) for at least 60 min at room temperature. Blocking buffer was removed and membranes were briefly washed with TBST. Antibodies against phospho-SMAD1/5/8 (13820 Cell Signaling), phospho-p44/42 MAPK (4370 Cell Signaling), SMAD1 (6944 Cell Signaling), GAPDH (2118 Cell Signaling) were then applied at a dilution of 1:1000, 1:2000 for GAPDH, in 1.0% BSA TBST and incubated at 4°C for 12 to 16 hr. After incubation with primary antibody, immunoblots were washed with TBST three times for 5 min at room temperature and a secondary antibody conjugated with horseradish peroxidase (7074 Cell Signaling) was applied to the blots at 1:1000 in 1.0% BSA TBST for 60 min at room temperature. After incubation with the secondary antibody, the immunoblots were washed with TBST three times for 5 min and developed using a luminol based substrate (7003 Cell Signaling). The immunoblots were imaged using a BioRad ChemiDoc MP imaging system using exposure times that produced signal below saturation. Densitometry was performed using ImageJ (<https://imagej.nih.gov>).

BMPR2

For assessment of BMPR2 protein expression after addition of select BMP ligands, cells were plated at 40% confluence under standard conditions in 24 well plates. Media was replaced, with addition of BMP9 (400ng/ml), and cells were then incubated at 37°C for the specified times. Cells were then treated with 50 μ l lysis buffer (see above). Samples were immediately stored at -80°C until processed for SDS-PAGE. After electrophoresis, gels were incubated with 20% ethanol in TBS for 5 min. Transfer of protein to nitrocellulose was performed with the iBlot apparatus using program 3 for 8 min. Antibodies against BMPR2 (6979 Cell Signaling) and GAPDH (2118 Cell Signaling) were then applied at 1:1000 and 1:2000, respectively, in 1.0% BSA TBST and incubated at 4°C for 12 to 16 hr. Immunoblots were processed, developed, and analyzed as described above.

BMP response with heparinase I/III

Cells were plated at 40% confluence in 96 well plates and cultured under standard conditions for 12 hr. Media was exchanged with media containing 2 units of Heparinase I/III (H3917 SIGMA) and cells were incubated at 37°C for 3 hr. Media was then replaced with media containing ligands at the specified concentrations. The cells were then incubated with ligands at 37°C for 20 min. After incubation for 20 min the cells were processed for phospho-SMAD1/5/8 staining and flow cytometry as described above.

BMP response with NaClO₃

Sensor cells were plated at 40% confluence under standard conditions including 20 mM NaClO₃ (Sigma) and passaged 36 hr later at 40% confluence in 96 well plates under the same conditions and cultured for another 12 hr. Media was then replaced and ligands were added at the specified concentrations. The cells were then incubated with ligands at 37°C for 24 hr and were processed for flow cytometry as previously described.

Receptor overexpression

Overexpression plasmids were constructed for each of the BMP receptors (BMPR1A, BMPR1B, BMPR2, ACVR1, ACVR2A, ACVR2B and ALK1) using the Gibson cloning method (Gibson et al., 2009). Bmp1b and Alk1 cDNA was purchased from Dharmacon (MMM1013-202858407 and MMM1013-202763719). All other receptor cDNAs were generated by RT-PCR from total RNA extracted from NMuMG cells. The receptor cDNA was concatenated with mTurquoise with an intervening T2A cleavage site (Szymczak and Vignali, 2005), and was expressed under the control of a constitutive PGK promoter integrated in the Pb510b plasmid backbone to enable PiggyBac integration (Ding et al., 2005; Wu et al., 2006). Stable integrations were then generated using the PiggyBac method. Cells were co-transfected with these overexpression plasmids and PB200A to express transposase, and selected with Geneticin. Experiments were performed with polyclonal populations resulting from PiggyBac integrations.

siRNA induced knock-down

Cells were plated at 40% confluence with 30 μ M total siRNA (ThermoFisher silencer select #4390771) and 3 μ l RNAiMAX (Life technologies). For every gene, a pool of two distinct siRNAs was used, listed in Table S3. Cells were passaged after 24 hr and were used for the relevant experiments.

Quantitative PCR

Total RNA was harvested from cell lysate using the RNeasy mini kit (QIAGEN) and cDNA was generated from 1 μ g of RNA using the iScript cDNA synthesis kit (BioRad) following the manufacturer's instructions. Primers and probes for specific genes (Table S4) were purchased from IDT. Reactions were performed using 1:40 dilution of the cDNA synthesis product with either IQ SYBR Green Super-mix or SsoAdvanced Universal probes Supermix (BioRad). Cycling was carried out on a BioRad CFX96 thermocycler using an initial denaturing incubation of 95° for 3 min followed by 39 cycles of (95°C for 15 s, followed by 60°C for 30 s). Each condition was assessed with two biological repeats and each reaction was run at least in triplicate.

Antibody detection for phospho-SMAD1/5/8

Cells exposed to specified concentrations of BMP4 for 24 hr were harvested from single wells of a 24 well plate using either 0.05mL Accutase (ES cells) or trypsin (NMuMG and 3T3 cells). Protease activity was quenched by re-suspending the cells in 0.45mL HBSS with 1.0% Bovine Serum Albumin (BSA). The cells were then pelleted, washed with 0.5mL PBS, and fixed by re-suspension in 0.5mL of 4.0% formaldehyde for 5 min at room temperature. Following fixation, the cells were washed in 0.5mL PBS and re-suspended in 0.5mL PBS with 1.0% Triton X-100 for permeabilization. The cells were then washed with 0.5mL PBS and re-suspended in blocking solution (PBS with 1.0% BSA and 0.1% Tween 20). Blocking was carried out for 30 min at room temperature. The cells were then pelleted and re-suspended in binding solution (PBS with 1.0% BSA) containing a 1:100 dilution of a primary antibody against the phosphorylated form of SMAD1/5/8 complex (Cell Signaling Technologies Cat# 13820). The staining proceeded for 12 – 16 hr at 4°C with constant rocking. Afterward, cells were washed with 0.5mL PBS and re-suspended in binding solution containing a 1:500 dilution of a secondary antibody labeled with Alexa 594 (#A21207, ThermoFisher). Secondary detection proceeded for 60 min at room temperature with constant rocking. Finally, cells were then pelleted, washed with 0.5mL PBS filtered with a 40 μ m mesh and analyzed by flow cytometry.

Time-lapse imaging

Fluorescent reporter cells were first mixed with an excess of non-fluorescent parental cells at a 1:9 ratio to simplify image segmentation and data extraction. Cells were then plated at $1.6 \cdot 10^4$ cells/well in a 96 well plate equivalent roughly to 15%–20% confluence. Cells were grown for 12 hr prior to ligand addition. Each position was imaged every hour starting from the addition of ligands until cells became confluent after about 60 hr. Images were then analyzed for the number of fluorescent cells and fluorescent signal level.

Mathematical model for promiscuous interactions

Many signalling pathways comprise multiple ligand and receptor variants that interact promiscuously with one another, with varying affinities, to form many distinct signalling complexes. BMP provides a canonical example of this architecture. However, other pathways, including TGF- β (SMAD2/3) signaling, FGF, Wnt, and JAK/STAT, also exhibit similar features. Here we develop a general mathematical model that captures essential aspects of receptor-ligand promiscuity in signalling pathways, and analyze it to understand the functional capabilities this architectural feature provides for cellular signal processing. This model focuses on several features of the natural BMP pathway: promiscuous ligand-receptor interactions, heterodimeric receptors (a simplified version of the natural Type I-Type II receptor tetramers), and variation in the activities of different signalling complexes. To focus on the signal-processing capabilities at the level of receptor-ligand interactions, we neglect other known features of the pathway including preliminary enzymatic processing of ligands, non-canonical signaling, downstream feedback loops (e.g., through SMAD6/7), and crosstalk with other signalling pathways. We specifically point out that while this model focuses on mixtures of ligand species, each ligand type is composed of two subunits. Thus the model can be used equally well for mixtures of homodimers, heterodimers, or combinations

thereof. Finally, we note that while the model applies most directly to the BMP pathway, variants of it could also describe other systems that similarly form multi-part signaling complexes, including receptor aggregates, such as those listed above.

We consider a system with n_L ligands, L_j , each of which can bind to one of n_A type A receptor subunits, A_i , to form $n_L \cdot n_A$ intermediate dimeric ligand-type A receptor complexes, D_{ij} . These complexes can in turn bind to one of n_B type B receptor subunits, B_k , to form $n_L \cdot n_A \cdot n_B$ different trimeric signaling complexes, T_{ijk} . We assume that the reactions are reversible where the kinetics are first-order in each reactant, with forward reaction rates given by $k_f^{D_{ij}}$ and k_f^T for the formation of dimeric and trimeric complexes, respectively, and with reverse reaction rates similarly given by $k_r^{D_{ij}}$ and k_r^T . These reactions can be summarized as follows



Next, we can write the dynamical equations that describe these reactions:

$$\frac{dL_j}{dt} = \frac{1}{V} \sum_{i=1}^{n_A} (-k_f^{D_{ij}} A_i L_j + k_r^{D_{ij}} D_{ij}) \quad (\text{Equation 3})$$

$$\frac{dA_i}{dt} = \sum_{j=1}^{n_L} (-k_f^{D_{ij}} A_i L_j + k_r^{D_{ij}} D_{ij}) \quad (\text{Equation 4})$$

$$\frac{dD_{ij}}{dt} = k_f^{D_{ij}} A_i L_j - k_r^{D_{ij}} D_{ij} + \sum_{k=1}^{n_B} (-k_f^T D_{ij} B_k + k_r^T T_{ijk}) \quad (\text{Equation 5})$$

$$\frac{dB_k}{dt} = \sum_{i=1}^{n_A} \sum_{j=1}^{n_L} (-k_f^T D_{ij} B_k + k_r^T T_{ijk}) \quad (\text{Equation 6})$$

$$\frac{dT_{ijk}}{dt} = k_f^T D_{ij} B_k - k_r^T T_{ijk}. \quad (\text{Equation 7})$$

Here, L_j denotes the concentration of the ligand in a volume V , and A_i , B_k , D_{ij} and T_{ijk} are the absolute number of receptors and complexes on the cell surface. We assume here that production and consumption are in a steady state enabling us to neglect the consumption of receptors and ligands by endocytosis. Subunits combine to form various complexes; however, the principle of conservation of mass requires that the total number of each type of molecule remain constant:

$$L_j^0 = L_j + \frac{1}{V} \left(\sum_{i=1}^{n_A} D_{ij} + \sum_{i=1}^{n_A} \sum_{k=1}^{n_B} T_{ijk} \right) \quad (\text{Equation 8})$$

$$A_i^0 = A_i + \sum_{j=1}^{n_L} D_{ij} + \sum_{j=1}^{n_L} \sum_{k=1}^{n_B} T_{ijk} \quad (\text{Equation 9})$$

$$B_k^0 = B_k + \sum_{i=1}^{n_A} \sum_{j=1}^{n_L} T_{ijk}, \quad (\text{Equation 10})$$

where L_j^0 is the total ligand concentration and A_i^0 and B_i^0 are the total receptor levels. Finally, each complex T_{ijk} induces phosphorylation of the intracellular signal, S , at some rate ϵ_{ijk} so that the rate of change of the total signal is given by

$$\frac{dS}{dt} = \sum_{i=1}^{n_A} \sum_{j=1}^{n_L} \sum_{k=1}^{n_B} \epsilon_{ijk} T_{ijk} - \gamma S. \quad (\text{Equation 11})$$

We consider the case where the volume for the ligand is large such that there are significantly more ligand molecules than receptors, which can be expressed by $V \rightarrow \infty$. This reflects our experimental conditions where the ligands are dissolved within a large excess of cell culture media. With this assumption Equations 3 and 8 decouple and become

$$L_j = L_j^0. \quad (\text{Equation 12})$$

Additionally, since binding and unbinding occur on fast timescales (minutes (Heinecke et al., 2009)) compared to the timescales of reporter expression, we focused on the behavior of this system at steady state. In this regime, all time derivatives in Equations 4–7 vanish and the system can be solved to give

$$D_{ij} = K_{ij}^D A_i L_j \quad (\text{Equation 13})$$

$$T_{ijk} = K_{ijk}^T D_{ij} B_k \quad (\text{Equation 14})$$

where we define $K_{ijk}^T \equiv K_{f_{ijk}}^T / K_{r_{ijk}}^T$, and $K_{ij}^D \equiv K_{f_{ij}}^D / K_{r_{ij}}^D$. Stronger affinity thus corresponds to larger values of the K 's. Similarly, setting Equation 11 to zero we get

$$S = \sum_{i=1}^{n_A} \sum_{j=1}^{n_L} \sum_{k=1}^{n_B} \epsilon_{ijk} T_{ijk}, \quad (\text{Equation 15})$$

with $\epsilon_{ijk} \equiv \epsilon_{ijk} / \gamma$. Therefore, the final system of equations describing our model is given as follows

$$A_i^0 = A_i + \sum_{j=1}^{n_L} D_{ij} + \sum_{j=1}^{n_L} \sum_{k=1}^{n_B} T_{ijk} \quad (\text{Equation 16})$$

$$B_k^0 = B_k + \sum_{i=1}^{n_A} \sum_{j=1}^{n_L} T_{ijk} \quad (\text{Equation 17})$$

$$D_{ij} = K_{ij}^D A_i L_j \quad (\text{Equation 18})$$

$$T_{ijk} = K_{ijk}^T D_{ij} B_k \quad (\text{Equation 19})$$

$$S = \sum_{i=1}^{n_A} \sum_{j=1}^{n_L} \sum_{k=1}^{n_B} \epsilon_{ijk} T_{ijk}. \quad (\text{Equation 20})$$

This system comprises a set of $N_v = n_A + n_B + n_A(1 + n_B)n_L + 1$ variables and $N_p = n_A + n_B + n_A(1 + 2 * n_B)n_L$ parameters.

Solving the steady-state equations

In order to find the total signal, S , we first need to solve the system of equations to find T_{ijk} . Plugging Equation 18 into Equation 16 we find

$$A_i \left(1 + \sum_{j'=1}^{n_L} K_{ij}^D L_{j'} \right) = A_i^0 - \sum_{j'=1}^{n_L} \sum_{k'=1}^{n_B} T_{ij'k'}$$

$$A_i = \frac{A_i^0 - \sum_{j'=1}^{n_L} \sum_{k'=1}^{n_B} T_{ij'k'}}{1 + \sum_{j'=1}^{n_L} K_{ij'}^D L_{j'}}. \quad (\text{Equation 21})$$

This can be used to solve for D_{ij}

$$D_{ij} = K_{ij}^D \frac{A_i^0 - \sum_{j'=1}^{n_L} \sum_{k'=1}^{n_B} T_{ij'k'}}{1 + \sum_{j'=1}^{n_L} K_{ij'}^D L_{j'}} L_j \quad (\text{Equation 22})$$

which we can plug into [Equation 19](#) to get a coupled set of $N = n_A \cdot n_L \cdot n_B$ quadratic equations for T_{ijk}

$$T_{ijk} = K_{ijk}^T K_{ij}^D \left(\frac{A_i^0 - \sum_{j'=1}^{n_L} \sum_{k'=1}^{n_B} T_{ij'k'}}{1 + \sum_{j'=1}^{n_L} K_{ij'}^D L_{j'}} \right) L_j \left(B_k^0 - \sum_{i'=1}^{n_A} \sum_{j'=1}^{n_L} T_{i'j'k'} \right). \quad (\text{Equation 23})$$

Solving [Equation 23](#), we can then obtain the signal S using [Equation 20](#).

The error function and least square minimization

In order to solve [Equation 23](#), we minimize an error function, defined as follows:

$$E(T_{ijk}) \equiv \sum_{i=1}^{n_A} \sum_{j=1}^{n_L} \sum_{k=1}^{n_B} \left[K_{ijk}^T K_{ij}^D \left(\frac{A_i^0 - \sum_{j'=1}^{n_L} \sum_{k'=1}^{n_B} T_{ij'k'}}{1 + \sum_{j'=1}^{n_L} K_{ij'}^D L_{j'}} \right) L_j \left(B_k^0 - \sum_{i'=1}^{n_A} \sum_{j'=1}^{n_L} T_{i'j'k'} \right) - T_{ijk} \right]^2. \quad (\text{Equation 24})$$

Here, E is a function of the complete set of T_{ijk} 's. It is always positive, being a sum of squares, and vanishes if and only if T_{ijk} is a solution to [Equation 23](#), which can now be written as

$$E(T_{ijk}) = 0. \quad (\text{Equation 25})$$

This equation is now in a form that can be solved numerically for any given set of parameters via standard optimization methods such as MATLAB's `fmincon` and `lsqnonlin` functions.

Dimensional reduction

The system of equations describing our model can be simplified by dimensional reduction, in which we redefine the variables to reduce the number of parameters and make the remaining parameters dimensionless.

First, we change the units of signal strength using a scaling factor, α .

$$\begin{aligned} S &\rightarrow \alpha \cdot S \\ \varepsilon_{ijk} &\rightarrow \alpha \cdot \varepsilon_{ijk}. \end{aligned} \quad (\text{Equation 26})$$

By choosing a value of $\alpha = (\sum_{i,j,k} \varepsilon_{ijk})^{-1}$, we can obtain units such that the phosphorylation rate constants for all complexes sum to 1:

$$\sum_{i,j,k} \varepsilon_{ijk} = 1. \quad (\text{Equation 27})$$

Similarly, changing the receptor units by rescaling with a factor β gives rise to the following transformation:

$$\begin{aligned} A_i &\rightarrow \beta \cdot A_i \\ B_k &\rightarrow \beta \cdot B_k \\ D_{ij} &\rightarrow \beta \cdot D_{ij} \\ T_{ijk} &\rightarrow \beta \cdot T_{ijk} \\ S &\rightarrow \beta \cdot S \\ K_{ijk}^T &\rightarrow \beta^{-1} \cdot K_{ijk}^T. \end{aligned} \quad (\text{Equation 28})$$

By choosing $\beta = \sum_{i,j,k} K_{ijk}^T$ we effectively obtain units for the receptors and receptor complexes in which the K_{ijk}^T sum to 1:

$$\sum_{i,j,k} K_{ijk}^T = 1. \quad (\text{Equation 29})$$

Finally, we can also independently choose new units for each individual ligand species:

$$\begin{aligned} L_i &\rightarrow \gamma_j \cdot L_i \\ K_{ij}^D &\rightarrow \gamma_j^{-1} K_{ij}^D \end{aligned} \quad (\text{Equation 30})$$

We can make these dimensionless by choosing $\gamma_j = \sum_i K_{ij}^D$, such that for every j ,

$$\sum_i K_{ij}^D = 1. \quad (\text{Equation 31})$$

Using these re-scaled variables and parameters, we can explore the complete parameter space by examining only parameter values satisfying Equations 27, 29, and 31. These constraints reduce the number of independent parameters, N_p , by $2 + n_L$.

The (2,2,2) model and parameter selection

In order to see what behaviors arise from the model of promiscuous interactions, we focused on a specific instantiation of the model with $n_L = 2$ ligands, $n_A = 2$ A-type receptors and $n_B = 2$ B-type receptors, which we describe as the (2,2,2) model. In this case there are 20 independent biochemical parameters, K_{ij}^D , K_{ijk}^T , and ε_{ijk} , restricted by Equations 27, 29, and 31, and 4 receptor expression level parameters A_i^0 and B_k^0 . In order to study all possible behaviors, random sets of parameters were chosen. We chose random biochemical parameters distributed uniformly over the bounded domains defined by Equations 27, 29, and 31, while the receptor parameters were chosen from a log-uniform distribution in the range $[10^{-3}, 10^3]$. Simulations were performed for 100,000 random parameter sets, and an entire 2D input-output function, across 15×15 log-uniform ligand concentrations, was numerically computed for each set. Results are plotted in Figure S4A.

Phenotypical parameters

A useful representation of the modeling results can be achieved by extracting parameters that measure phenotypic characteristics of the computation performed for each of the parameter sets. In this study we focused on two such parameters, the relative ligand strength (RLS) and the ligand interaction coefficient (LIC), as diagrammed in Figure S4B–D. More specifically, we define RLS as follows:

$$\text{RLS} = \frac{S_{\text{weak}}}{S_{\text{strong}}}, \quad (\text{Equation 32})$$

where S_{strong} and S_{weak} are the activation strengths of the pathway when induced by the stronger or weaker ligand individually, at saturating levels. In the case where one ligand is a potent activator while the second ligand is weak this index drops to 0. However, when both ligands individually activate the pathway to a similar extent, this index approaches 1.

LIC measures the effective interaction between the ligands at high ligand concentration ($L_i \gg 1$). We define the satmax and satmin functions to be the maximal or minimal response, respectively, over varying ligand ratios, at saturating total ligand concentrations (Figure S4B–S4D). Using these functions, the ligand interference index can be defined as

$$\text{LIC} = \frac{\text{satmin}(S)}{S_{\text{weak}}} - \frac{S_{\text{strong}}}{\text{satmax}(S)}. \quad (\text{Equation 33})$$

For non-interacting ligands, we expect that mixed levels of ligands produce responses that lie within the range defined by the effects of the individual ligands, in which case the coefficient vanishes. However, if a combination of ligands gives rise to a stronger response than that of the stronger ligand individually, the first term generates a positive value for this index. On the other hand, if the response to a combination of ligands is smaller than the weaker ligand, the second term dominates, and the index becomes negative. The range for this index is therefore $[-1, 1]$.

The four archetypes and the structure of parameter space

Plotting the values of LIC and RLS for each simulation, we find that the response profiles form a continuous distribution that interpolates between 4 archetypal computations (Figures 4C and S4E). These archetypal computations generally map to different regions in parameter space. Here we describe in more detail the parameter regimes that give rise to each of these archetypes.

Additive (Figure S6A)

The additive integration can be thought of as the “default” computation. It occurs when both ligands have equivalent receptor affinities ($K_{i1}^D \sim K_{i2}^D$, $K_{i1k}^T \sim K_{i2k}^T$) and they produce equivalently active complexes ($\varepsilon_{i1k} \sim \varepsilon_{i2k}$). In such a regime, similarly active complexes form regardless of whether one ligand, the other, or both are present, and thus, the response does not depend on the composition of the ligands but only on the total ligand concentration in the environment. This simple computation can occur even when there is only a single receptor variant ($n_A = n_B = 1$).

Ratiometric (Figure S6B)

Ratiometric computation occurs when the ligands produce signaling complexes with significantly different activity levels ($\varepsilon_{i1k} \gg \varepsilon_{i2k}$). When L_1 is present, high activity complexes (T_{i1k}) form and the pathway is strongly activated. In contrast, when only

L_2 is present, only low activity complexes (T_{12k}) form and the pathway is weakly activated. In a mixed environment, L_2 will compete with L_1 for receptor binding, competitively inhibiting formation of the more active complexes, and thus reducing pathway activation below its maximal level in a ratiometric manner. Note that this computation can also occur with only a single receptor variant ($n_A = n_B = 1$), and that similar ratiometric sensing behaviors have been observed in other systems (Atkinson, 1968; Berg et al., 2009; Escalante-Chong et al., 2015; Madl and Herman, 1979).

Imbalance detection (Figure S6C)

Imbalance detection can be thought of as a combination of two opposing ratiometric computations, and thus requires the existence of at least two receptor variants, A_1 with $\varepsilon_{11k} \gg \varepsilon_{12k}$ and A_2 with $\varepsilon_{21k} \ll \varepsilon_{22k}$. Moreover, receptor-ligand affinities should be such that each receptor preferentially binds to the ligand with which it forms the weaker complex, i.e., $K_{11}^D < K_{12}^D$ and $K_{22}^D < K_{21}^D$. In this regime, when only a single ligand is present, it can bind both type A receptors, leading to formation of both the more active and less active signaling complexes. However, when both ligands are present simultaneously, they compete for type A receptor, producing primarily the high affinity signaling complexes, which, in this regime, are precisely those with weaker activity. Thus, in this case, the ligands effectively reduce each other's ability to activate the pathway.

Balance detection (Figure S6D)

Balance detection occurs in a similar way as the imbalance modes, except that the affinities favor the formation of the more active signaling complexes. We still have $\varepsilon_{11k} \gg \varepsilon_{12k}$ and $\varepsilon_{21k} \ll \varepsilon_{22k}$, as with imbalance detection. However, for this computation, $K_{11}^D > K_{12}^D$ and $K_{22}^D > K_{21}^D$, such that higher affinity receptor-ligand pairs now correspond to the higher activity complexes. Consequently, as before, a mixture of ligands will produce mostly the higher affinity complexes (T_{11k} and T_{22k}), but now these complexes have higher, rather than lower, activity.

Furthermore, the balance detection effect can be enhanced by further reducing the activating effects of individual ligands. Consider the case where only L_1 is present. Lack of competition enables binding of L_1 to both type A receptors giving rise to D_{11} and D_{21} . If affinities of these dimeric complexes for B-type receptors obey $K_{11k}^T < K_{21k}^T$, then there will be more trimeric complexes of the form T_{21k} than T_{11k} . Assuming the high activity complexes are similarly active to each other, $\varepsilon_{11k} \sim \varepsilon_{22k}$, then $\varepsilon_{21k} \ll \varepsilon_{11k}$, and therefore, the enrichment for T_{21k} will tend to decrease the total signal, further enhancing the balance detection effect.

Computations depend only on ligand ratios at high ligand concentrations

A striking feature of the computations performed by the ligand-receptor interactions (Figure S4A) is the appearance of diagonal contours in the log-log ligand space. These reflect a general dependence of output on ratios of the two ligands. In fact, this behavior is more general, occurring for any number of ligands and receptors, and can be understood from the model. This can be seen by examining Equation 23, where the ligand dependence is entirely through the factor

$$\frac{L_j}{1 + \sum_{j'=1}^{n_L} K_{ij'}^D L_{j'}} = \frac{1}{\frac{1}{L_j} + \sum_{j'=1}^{n_L} K_{ij'}^D R_{jj'}}. \quad (\text{Equation 34})$$

Here, on the right-hand side, we have introduced $R_{jj'} \equiv L_{j'}/L_j$ to represent the ratios between each pair of ligands. When ligand concentrations are large, $L_j \gg 1$, the $1/L_j$ vanishes and the solution depends only on ratios between ligands and not on their absolute levels.

Archetypal computations differ from Boolean logic gates

It is also interesting to note that the previous observation suggests a significant distinction between the observed computations, e.g., the archetypes in Figure 4, and Boolean logic functions. Superficially, the additive, imbalance and balance computations resemble Boolean OR, XOR, and AND gates, respectively. However, a key feature of Boolean logic is the existence of threshold levels that can be used to binarize inputs. For example, to behave like a Boolean AND gate, one would expect that when both inputs are each above some threshold, the output should always be “on.” By contrast, in the computations analyzed here, no such thresholds exist. For example, in an imbalance detection mode, consider two ligand concentrations L_1 and L_2 that individually activate, but produce a weaker response together, i.e., appear to represent two “high” input levels that together produce a “low” output. Because output depends only on ligand ratios, for any value of L_1 chosen here, we can find a concentration of the second ligand, $L'_2 > L_2$ that will decrease the ligand ratio enough to generate a “high” output. Similar considerations apply for the balance detection computation.

Biological parameter range

In our analysis of model response profiles, we selected random values for dimensionless parameters, distributed across the entire theoretical possible range. This allowed us to understand the full repertoire of theoretically possible responses. We then restricted the analysis to biologically plausible values for each of the parameters to constrain the analysis to biologically relevant regimes. For receptor expression, based on previous measurements of the number of TGF-β receptors in different cell lines (Wakefield et al., 1987), we chose the total receptor counts A_i^0 and B_k^0 in a log-uniform distribution in the range $[0, 9 \cdot 10^4]$. For the ligand levels L_i^0 , we considered the range of experimentally utilized ligand concentrations: $[10^{-1}, 10^3]$ ng/ml. To make it comparable with the units for the receptor we converted this range to units of molecules, assuming a typical molecular weight for BMP ligands of about

30 kDa. This produced a concentration range of $[10^{-12}, 10^{-8}]$ M. Multiplying by a typical eukaryotic cell volume of $2 \cdot 10^3 \mu\text{m}^3$, we estimate ligand numbers per cell volume in the range of $[1, 10^4]$ molecules.

When receptors and ligands are measured in number of molecules, the affinity parameters K_{ij} and K_{ijk} have units of molecule $^{-1}$ (i.e., per molecule). Using estimates in the literature based on surface plasmon resonance measurements (Aykul and Martinez-Hackert, 2016), as well as theoretical models (Nicklas and Saiz, 2013), we conservatively selected affinities from a log-uniform distribution over the range $[10^{-3}, 10^{-1}]$. Finally, the efficiency parameters ε_{ijk} have arbitrary units that define the scale of the response and thus were chosen uniformly in the range $[0, 1]$ without loss of generality.

Using these ranges, we selected 100,000 random parameter sets and performed simulations to compute the input-output functions for each parameter set across a 9×9 matrix of ligand concentrations. The results show that a full range of response profiles could occur (Figures S5C and S5D). Further quantification of the relative frequencies of each response profile revealed a decreased frequency of ratiometric responses and increased frequencies of other functions, compared with the unrestricted parameter screen (Figure S5E).

Versatility search

A key aspect of the model is that it permits the cell to change the computation performed on a pair of ligands by modulating receptor expression. In order to study the effect of receptor expression levels on the computation performed, we selected 1000 random biochemical parameter sets. For each, we simulated the model with varying expression levels of each of the 4 receptor subunits (A_1, A_2, B_1, B_2) systematically chosen from a log-uniform distribution over the range $[10^{-3}, 10^3]$. The distribution of LIC and RLS values over the receptor expression levels was then calculated. These distributions were plotted for two specific biochemical parameter sets (one versatile and one non-versatile) in Figure 6A. The biochemical parameters are provided in Table S5.

Robustness to perturbations in receptor expression

Both theoretical and experimental analysis revealed that changes in receptor expression levels can reprogram the computation performed by cells. This observation provokes the question of how the computation could vary in response to fluctuations, or ‘noise’, in receptor expression levels (Elowitz et al., 2002).

We consider two types of fluctuations in receptor levels. First, there might be overall, correlated fluctuations across all receptors. Such extrinsic noise might reflect global changes in expression machinery, as well as fluctuations due to cell growth and division. Second, each receptor could vary stochastically in its expression, leading to independent fluctuations, or intrinsic noise. More quantitatively, we defined the receptor noise v as the coefficient of variation of receptor level. In addition, we defined α_E and α_I as the relative proportions of extrinsic and intrinsic noise, with $\alpha_E + \alpha_I = 1$.

To simulate the extrinsic noise, we generated a scale factor, s , drawn from a gamma distribution with shape parameter α_E/v^2 , and scale parameter v^2 (giving a mean of α_E and variance $\alpha_E v^2$). Similarly, intrinsic noise was simulated by choosing a receptor dependent scale factor s_i , drawn from a gamma distribution with shape parameter α_I/v^2 and scale parameter v^2 (mean α_I and variance $\alpha_I v^2$). To add noise to the receptor expression levels we multiplied the mean receptor level, R_i^0 , by a combined scale factor $(s + s_i)$. This combined scale factor has mean 1 and variance v^2 , giving rise to the desired coefficient of variation.

We then set out to analyze cellular sensitivity to receptor perturbation across the spectrum of ligand computations. We randomly chose 100 parameter sets from each of 5 regions in the phenotypic space defined by RLS and LIC. These regions were chosen to represent the additive ($-0.05 < \text{LIC} < 0.05$, $\text{RLS} > 0.8$), ratiometric ($-0.05 < \text{LIC} < 0.05$, $\text{RLS} < 0.2$), imbalance ($\text{LIC} < -0.1$, $\text{RLS} > 0.8$), and balance ($\text{LIC} > 0.1$, $\text{RLS} > 0.8$) archetypes, as well as an intermediate region ($-0.05 < \text{LIC} < 0.05$, $0.4 < \text{RLS} < 0.6$) that represented part of the spectrum of input-output functions but was not specifically associated with a single archetype. For each parameter set, we performed perturbations using 3 types of noise: purely extrinsic noise ($\alpha_E = 1, \alpha_I = 0$), purely intrinsic noise ($\alpha_E = 0, \alpha_I = 1$), or a combination of extrinsic and intrinsic noise ($\alpha_E = 0.5, \alpha_I = 0.5$). To enable comparison of the effects of each type of perturbation, we used a fixed coefficient of variation, $v = 0.25$.

Representative examples for each region (Figures S7D–S7F) show the spread of the resulting functions in phenotypic space. We find that extrinsic noise generates comparatively small quantitative changes in response profiles relative to intrinsic noise, with the combination of extrinsic and intrinsic noise showing an intermediate effect. To systematically characterize the variation in phenotypic space, we analyzed the distribution of the standard deviations of the change in RLS and LIC across all perturbations for each parameter set (Figures S7G and S7H). While these differences are generally insufficient to change the class of input-output function observed, we find that intrinsic noise produces greater variability in the phenotypic parameters. These results suggest that the observed input-output functions in the model of the BMP signaling pathway depend primarily on relative ratios of receptor levels rather than absolute numbers.

Finite volume of extracellular space

In the experimental context, cells were exposed to a large volume of media such that the total amount of ligand was much greater than the number of receptors. Using this high volume assumption results in constant ligand levels, even as they bind receptors to form active complexes (Equation 12). However, this regime might not necessarily be applicable to all *in vivo* contexts where the exact ratio of ligands to receptors could vary, and titration of ligands by receptors can affect their concentration. Therefore, it is noteworthy to consider also the case of a finite volume. Under these conditions, the steady-state equations, (Equations 16–20) become

$$L_j^0 = L_j + \sum_{i=1}^{n_A} D_{ij} + \sum_{i=1}^{n_A} \sum_{k=1}^{n_B} T_{ijk} \quad (\text{Equation 35})$$

$$A_i^0 = A_i + \sum_{j=1}^{n_L} D_{ij} + \sum_{j=1}^{n_L} \sum_{k=1}^{n_B} T_{ijk} \quad (\text{Equation 36})$$

$$B_k^0 = B_k + \sum_{i=1}^{n_A} \sum_{j=1}^{n_L} T_{ijk} \quad (\text{Equation 37})$$

$$D_{ij} = K_{ij}^D A_i L_j \quad (\text{Equation 38})$$

$$T_{ijk} = K_{ij}^T D_{ij} B_k \quad (\text{Equation 39})$$

$$S = \sum_{i=1}^{n_A} \sum_{j=1}^{n_L} \sum_{k=1}^{n_B} \varepsilon_{ijk} T_{ijk}. \quad (\text{Equation 40})$$

Plugging Equations 38 and 39 in 35–37 we get:

$$L_j^0 = L_j \left(1 + \sum_{i=1}^{n_A} K_{ij}^D A_i + \sum_{i=1}^{n_A} \sum_{k=1}^{n_B} K_{ijk}^T K_{ij}^D A_i B_k \right) \quad (\text{Equation 41})$$

$$A_i^0 = A_i \left(1 + \sum_{j=1}^{n_L} K_{ij}^D L_j + \sum_{j=1}^{n_L} \sum_{k=1}^{n_B} K_{ijk}^T K_{ij}^D L_j B_k \right) \quad (\text{Equation 42})$$

$$B_k^0 = B_k \left(1 + \sum_{i=1}^{n_A} \sum_{j=1}^{n_L} K_{ijk}^T K_{ij}^D A_i L_j \right), \quad (\text{Equation 43})$$

which can be numerically solved as before. We see that the distribution of behaviors remains similar with all four behaviors arising even in the finite volume regime (Figure S5A).

Additionally, one can also ask how the finite volume assumption impacts the computations. To test this, we considered both models for every set of parameters and compared the resulting behavior. While the two models give rise to qualitatively similar responses to increasing ligand levels, they differ specifically at intermediate ligand levels (Figure S5B), where the finite model produces a sharper dependence on ligand concentration, or, equivalently, a reduced input dynamic range.

Signaling modifiers

In addition to receptors and ligands, other secreted and cell bound proteins could in principle reshape the activity of pathway elements. In the BMP pathway many such modifiers are known, including secreted ligand-binding molecules (e.g., Twsg, Chordin, Noggin) and pseudo-receptors (e.g., BAMBI). While these factors were not explicitly modeled, they can be incorporated within the same formalism. Ligand binding molecules can generally form complexes with ligands, just as the receptors do. Therefore, mathematically they are equivalent to type A receptors, with affinities that can be specified in the corresponding elements of K_{ij}^D . Since these modifiers are secreted, the resulting complexes will not form complexes with type B receptors, and will not produce active signaling complexes. In the model, this can be represented by 0 values for the corresponding elements of both K_{ijk}^T and ε_{ijk} . We thus see that the secreted ligand-binding modifiers are mathematically equivalent to orphan type A receptors. Pseudo-receptors similarly have 0 values of ε_{ijk} , but could have non-zero values for K_{ijk}^T .

We therefore see that the modeling framework can naturally extend to include many biologically relevant components of the BMP pathway. While these elements do not play critical roles in the in vitro setting explored in this manuscript, they could play more important roles in vivo.

Nonlinear signal accumulation

Another assumption in the model is that the receptors all contribute linearly to the overall total phosphorylation rate (Equation 11). This assumption holds when the dephosphorylation rate is large compared with the phosphorylation rate, such that there is a large pool of dephosphorylated SMAD protein. A similar assumption was utilized in various models of the BMP and TGF- β pathway such as in (Vilar et al., 2006), and is motivated by experimental results of the TGF- β dependent phosphorylation and dephosphorylation rates (Inman et al., 2002). Since distinct cell types can differ in their kinase level, among others, it is biologically interesting to consider what happens in a regime where this assumption does not hold. The full equation describing the phosphorylated SMAD signal (S_p) should be written as

$$\frac{dS_p}{dt} = \sum_{i=1}^{n_A} \sum_{j=1}^{n_L} \sum_{k=1}^{n_B} \epsilon_{ijk} T_{ijk} S_u - \gamma S_p, \quad (\text{Equation 44})$$

where S_u is the amount of unphosphorylated SMAD and γ is the dephosphorylation rate. Using $S_{tot} = S_u + S_p$, we get

$$\frac{dS_p}{dt} = \sum_{i=1}^{n_A} \sum_{j=1}^{n_L} \sum_{k=1}^{n_B} \epsilon_{ijk} T_{ijk} (S_{tot} - S_p) - \gamma S_p. \quad (\text{Equation 45})$$

Solving for the steady-state solution one finds

$$S_p = \frac{\sum_{i=1}^{n_A} \sum_{j=1}^{n_L} \sum_{k=1}^{n_B} \epsilon_{ijk} T_{ijk}}{1 + \sum_{i=1}^{n_A} \sum_{j=1}^{n_L} \sum_{k=1}^{n_B} \epsilon_{ijk} T_{ijk}} S_{tot} \quad (\text{Equation 46})$$

where we define $\epsilon_{ijk} = \epsilon_{ijk}/\gamma$ as before. From this we see that for slow total phosphorylation rates, $\sum_{i=1}^{n_A} \sum_{j=1}^{n_L} \sum_{k=1}^{n_B} \epsilon_{ijk} T_{ijk} \ll 1$, we recover the linear behavior (Equation 20). However, when the phosphorylation rates become faster, compared to the characteristic dephosphorylation rate, the response reaches saturation. It is important to note that overall the signal is still determined by a monotonically increasing function of the weighted sum of all trimeric complexes. Therefore, while the quantitative nature of the computations can depend on the exact ratio between phosphorylation and dephosphorylation rates, the qualitative behaviors remain similar.

Additional features of the BMP pathway

The model above neglects a number of known features of the natural BMP pathway in order to focus on the specific effects of promiscuity, and to demonstrate its sufficiency for explaining observed computations. These other features are likely to play additional functional roles in the signaling pathway. One example is the dynamical nature of the receptor-ligand interactions, arising from receptor internalization, trafficking, and degradation. While the steady-state response studied in this paper is consistent with the BMP data, the parallel TGF- β branch of the pathway appears to respond transiently (adaptively) in some contexts (Warmflash et al., 2012). Alternative models (Vilar et al., 2006; Zi et al., 2012) were previously developed that focused on these dynamical aspects of the TGF- β response, and showed how these dynamics can give rise to either transient or sustained responses, as well as absolute or relative ligand response profiles, although not the balance and imbalance detection modes described here.

Spatial heterogeneity

The plasma membrane has been shown to contain microdomains differing in lipid and protein composition, or interactions with the cytoskeleton, which could in principle affect spatial and temporal receptor distribution (Delos Santos et al., 2015). This provokes the question of how receptor localization in microdomains could affect the computational behavior of the system. For example, a given receptor could be partially or completely segregated into certain domains which may or may not overlap with the localization of other receptors. Such effects can be modeled by replacing the existing affinity parameters with effective affinity parameters. Specifically, if two receptors are localized to completely different microdomains their effective affinity would be zero. By contrast, if they have a slight preference for distinct microdomains, their effective affinities would only be reduced. Representing domain preference this way provides two potential advantages for the system. First, it enables more flexibility in reaching diverse effective affinities among components. Second, if microdomain localization can be regulated by the cell, it can allow for dynamical tuning of effective affinity parameters, an additional mode of control.

QUANTIFICATION AND STATISTICAL ANALYSIS

Average and variability analysis

All single cell flow cytometry data were averaged by taking the population median. Repeats were averaged by taking the mean of at least 3 repeats. Variability was assessed either using standard deviation or standard error of the mean, as indicated in the legend. To remove bias due to day-to-day variability we normalized each repeat by an overall scale factor. This was determined using total least square fit between each two experiments.

Assignment of integration modes in survey

In the survey (Figure 2A), for each ligand pair, (L_1, L_2), five different combinations (Figure S1G) were measured: $L_1, L_2, L_1+L_2, L_1+L_1, L_2+L_2$, where the latter two indicate double the base concentration of a single ligand. Of these 5 combinations, the first three were assayed four times each, while the latter 2 were measured in duplicate. To estimate the relative likelihood of each ligand integration mode (Types I-IV in Figure S1G), we examined all 256 possible measurement combinations. For each one, we determined the corresponding integration mode based on the classification scheme in Figure S1G. The relative likelihoods were then estimated by calculating the frequency of each integration mode. This is plotted in Figure S1H, as shown in the inset.

RNaseq Analyses

Total RNA was collected from cells using the RNeasy Mini Kit (QIAGEN) following the manufacturer's instructions. Sequencing libraries were constructed using NEBNext Ultra RNA-seq kit (NEB #E7530) and sequenced on Illumina HiSeq2500. Results were then analyzed using the web-based Galaxy platform (<https://usegalaxy.org/>). Alignment was performed using the TopHat algorithm followed by transcript assembly and FPKM estimates using the Cufflinks algorithm.

DATA AND SOFTWARE AVAILABILITY

Flow cytometry data was analyzed in MATLAB using a custom software (EasyFlow). Mathematical model simulations were performed and analyzed in MATLAB. All the analysis code is available upon request (see Contact for Reagent and Resource Sharing).

The RNAseq data reported in this paper have been deposited with the accession number GEO: GSE98674.

Supplemental Figures

Cell

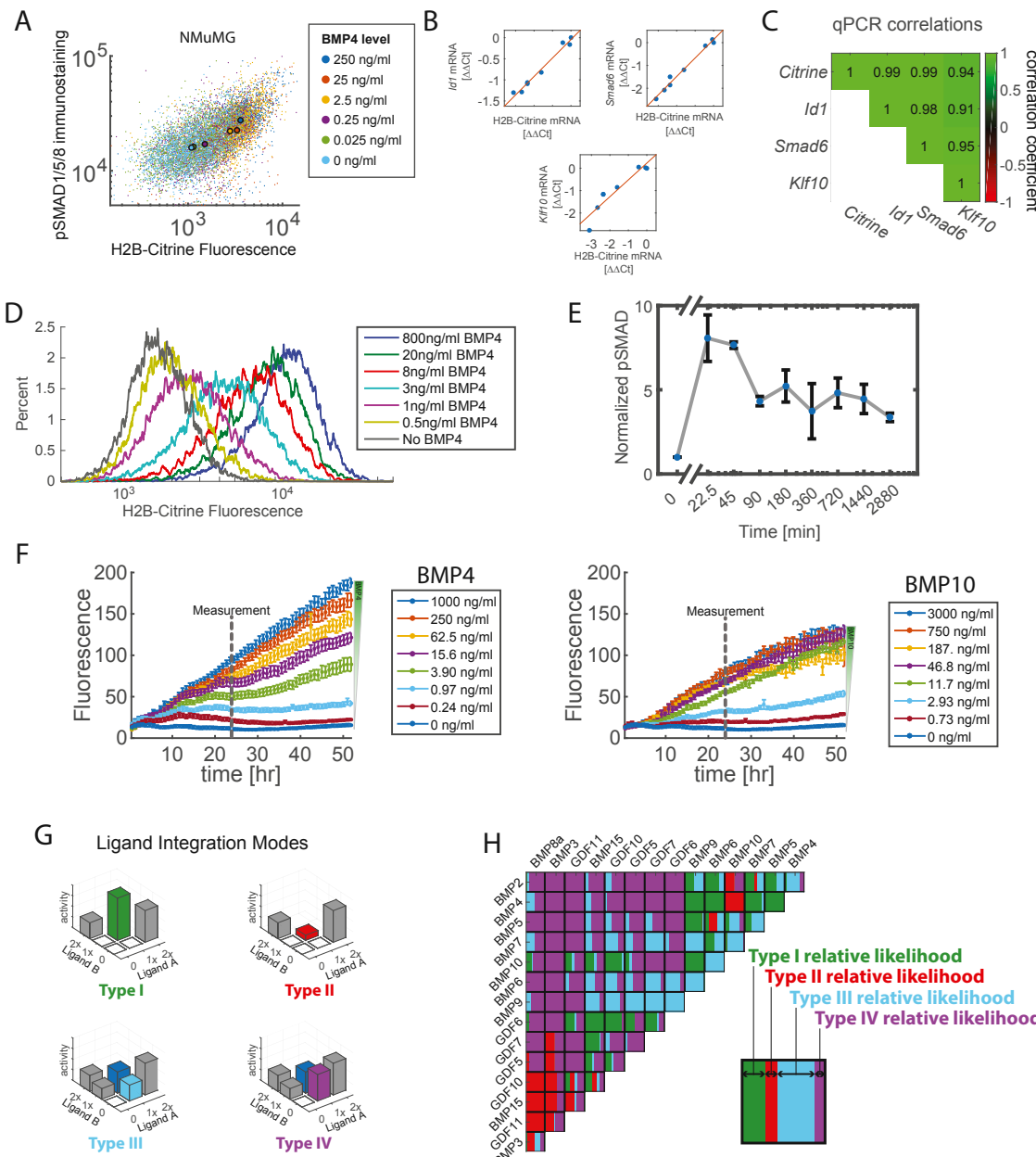


Figure S1. Ligand Pairs Can Show Complex Integration Modes, Related to Figure 2

- (A) NMuMG BMP reporter cells were stimulated with different concentrations of BMP4 (colored dots) and analyzed by flow cytometry for both reporter H2B-Citrine expression (x axis), and immunostaining of phosphorylated SMAD1/5/8 (y axis). Note strong correlation both within (scatter, single cells) and between (larger circles, population average) ligand concentrations.
- (B) qPCR measurements show endogenous BMP-responsive gene expression levels correlate with H2B-Citrine reporter expression. Plots show relationships between H2B-Citrine and specific indicated target genes.
- (C) Correlation coefficients for each pair of target genes shown in (B).
- (D) Flow cytometry of reporter H2B-Citrine expression showed unimodal distributions 24h after stimulation across the indicated range of BMP4 concentrations (colors).
- (E) Dynamics of phosphorylated SMAD1/5/8 were measured using immunoblotting at time-points up to 48 hr after BMP addition. After a short transient of a few hours, phosphorylated SMAD1/5/8 levels remained constant. The plot shows mean and SD (error bars) of 3 independent repeats.
- (F) Reporter cells were exposed to different concentrations of BMP4 (left) or BMP10 (right). Fluorescence was monitored using time-lapse microscopy over more than 48 hr. Continuous increases in mean fluorescence per cell occurred in most conditions. This result contrasts with the adaptive dynamics observed in response to stimulation by TGF- β ligands (Warmflash et al., 2012). Vertical dashed line indicates the 24 hr time point used for most experiments in the paper.

(legend continued on next page)

(G) 4 modes of ligand integration are shown schematically. Type I is characterized by a strong response to mixed ligands (green), with weaker responses to the individual ligands (gray). Type II is characterized by a weak response to mixed ligands (red), in comparison to individual ligands. In cases where the mixed response is intermediate (dark blue), two additional integration modes can be realized: The type III integration mode is characterized by decreased activity in response to removal of one ligand (dark blue to light blue). Finally, a type IV integration mode occurs when removal of one of the ligands causes an increase in the response (dark blue to purple).

(H) Using the low resolution ligand survey (Figure 2A), all pairs of ligands were classified across these 4 integration modes. For every pair, the likelihood of each mode was calculated ([STAR Methods](#)) and the corresponding square was colored by bands with widths proportional to the relative likelihood of each mode. The appearance of multiple colors in the same square thus indicates uncertainty about the integration mode.

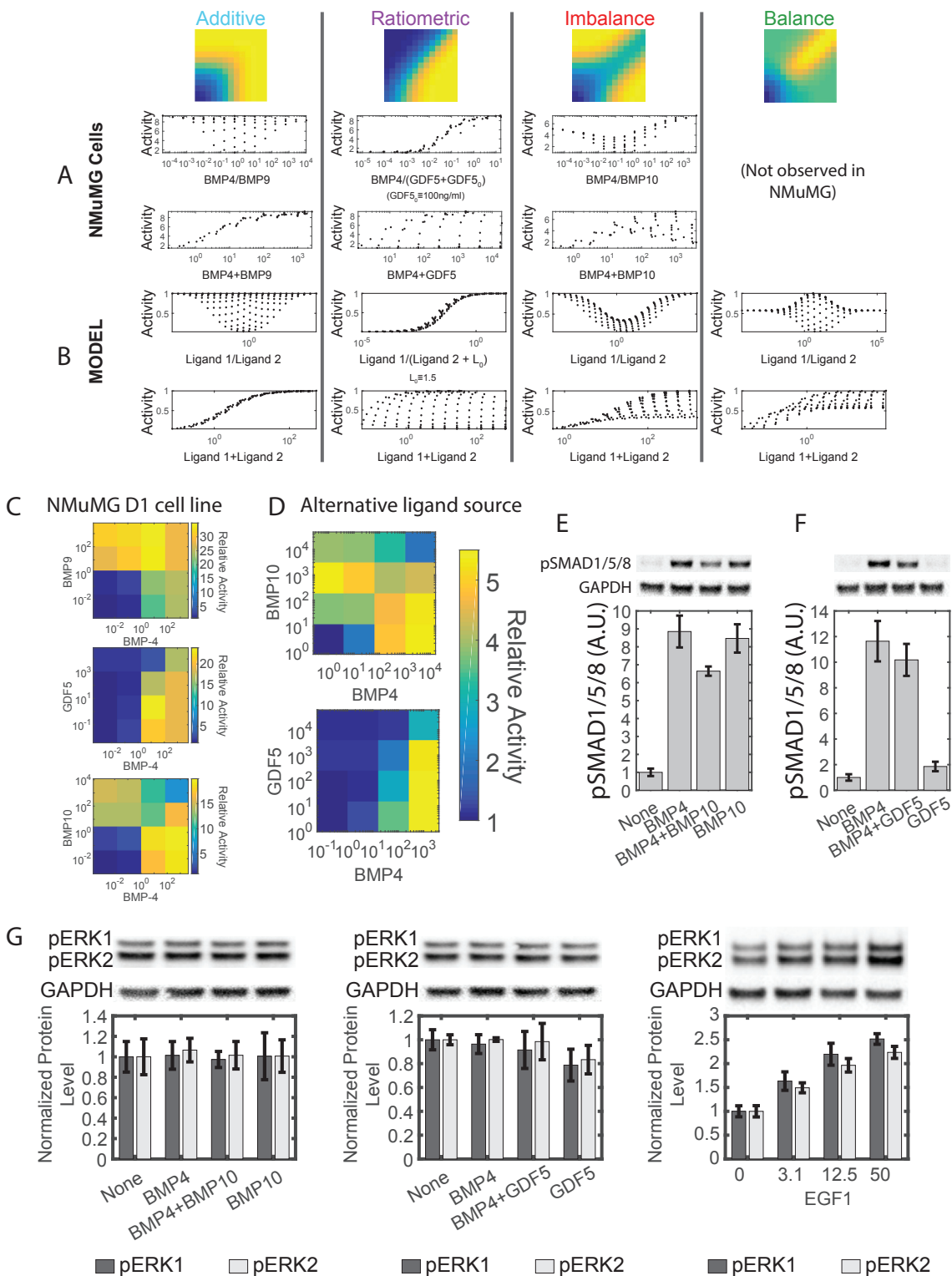


Figure S2. Cellular Response to Specific Relations between Ligands Can Be Seen Theoretically and Experimentally with Different Reporter Lines, Ligand Sources, and Readouts, Related to Figures 2 and 3

(A) For each ligand pair, experimentally measured pathway activity is plotted across all points in the ligand matrix, as a function of either the adjusted ratio of the two ligand concentrations (upper plot) or the sum of the two ligand concentrations (lower plot). Most of the variation in activity in BMP4-BMP9 can be explained by the sum of the two ligands (left plots). For BMP4-GDF5, the data are better explained as a function of an adjusted ratio, where the GDF5 concentration was offset

(legend continued on next page)

bioRxiv preprint doi: <https://doi.org/10.1101/2023.09.04.553700>; this version posted September 5, 2023. The copyright holder for this preprint (which was not certified by peer review) is the author/funder, who has granted bioRxiv a license to display the preprint in perpetuity. It is made available under a [CC-BY-ND 4.0 International license](https://creativecommons.org/licenses/by-nd/4.0/).

by a constant, representing the threshold above which the response becomes approximately ratiometric. For BMP4-BMP10, the response approximately follows a non-monotonic function of the ratio.

(B) Similar plots for the archetypes were generated in the model.

(C) An independent BRE-based sensor cell line was generated from NMuMG using a different integration technique (PiggyBac, [STAR Methods](#)). It was exposed to the same BMP ligand pairs, giving rise to similar combined responses (cf. [Figures 2C–2E](#)).

(D) Ligands acquired from a different source (Peprotech, [STAR Methods](#)), show similar responses to those acquired from R&D Systems (cf. [Figures 2D and 2E](#)).

(E and F) Phosphorylated SMAD1/5/8 was analyzed using immunoblotting in cells exposed to single ligand, ligand combinations, or no ligand. BMP4 and BMP10 exhibited imbalance detection (E), while BMP4 and GDF5 exhibited a ratiometric response (F).

(G) ERK phosphorylation in response to BMP ligands was analyzed using immunoblotting. While both ERK1 and ERK2 respond dose-dependently to EGF1, they show no response to BMP4, BMP10 and GDF5. In (E)–(G), results are normalized to the un-activated condition, and represent the mean and SD of at least 3 independent repeats.

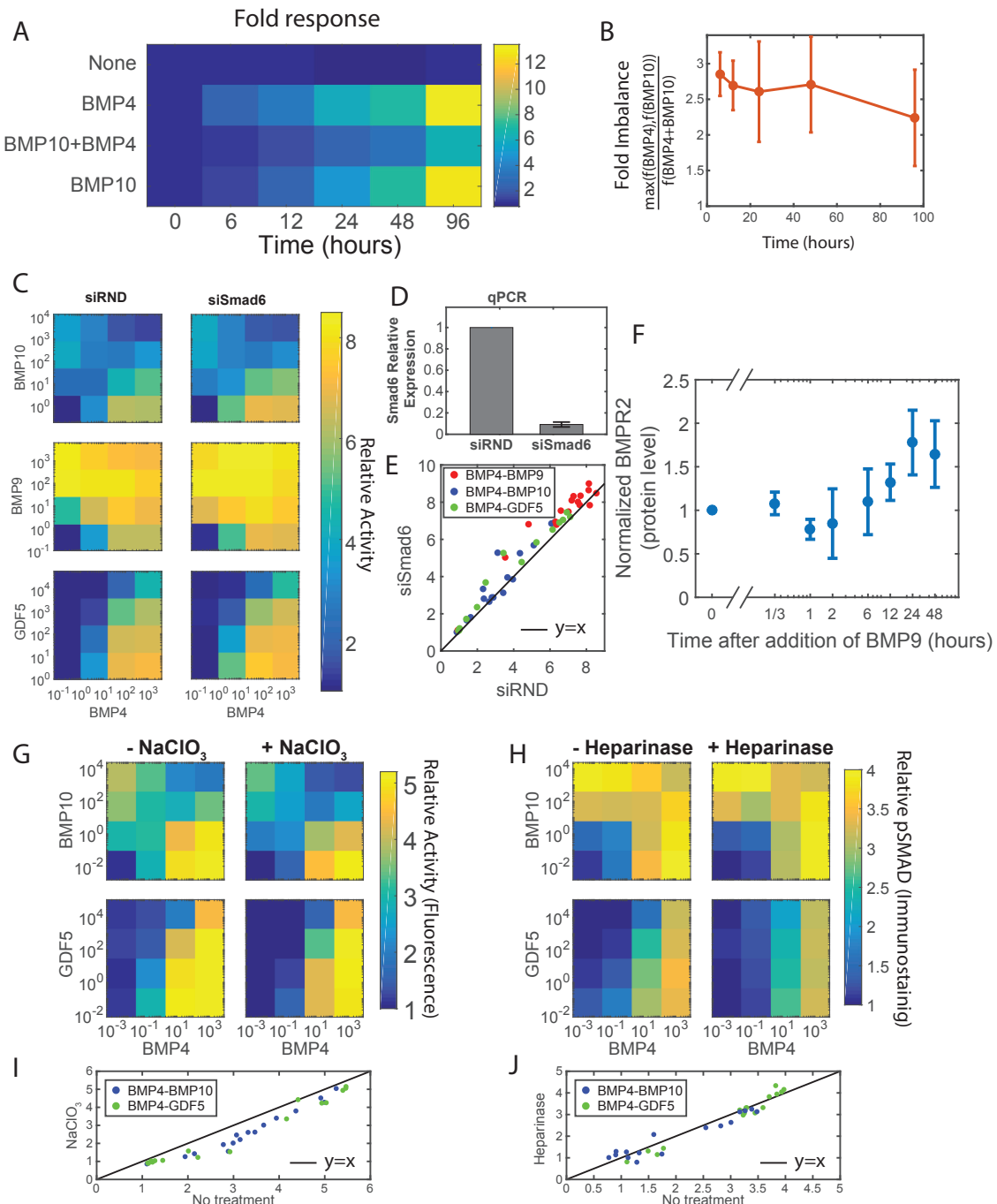


Figure S3. Ligand Response Profiles Are Stable over Time and in Response to Perturbations of Feedback Loops and HSPG Components, Related to Figure 3

(A) Cells were stimulated with combinations of BMP4 and BMP10. Pathway responses were analyzed at different time points after ligand addition. Absolute fluorescence levels increased over time. However, the imbalance response is visible at all time points, from 6 to 96 hr after stimulations.

(B) BMP4-BMP10 antagonism from (A) was quantified as the ratio of the least active individual ligand to activation by both ligands. This quantity was stable over the duration of the experiment. Error bars indicate SD calculated from three independent experiments.

(C–E) SMAD6 knockdown does not disrupt ligand integration. The input-output response is plotted for cells treated with siRNA against *Smad6* (siSmad6) or with a random sequence (siRND) (C). qPCR analysis shows that siRNA treatment reduced *Smad6* transcript by ~90% (D). Error bars indicate SD calculated from three independent experiments. The results with siRNA for *Smad6* were plotted against those with a random siRNA sequence (E). Each dot represents a single ligand combination. Different colors represent different ligand pairs and the black line represents the line $y = x$ for reference.

(legend continued on next page)

(F) Cells were stimulated with BMP9 and BMPR2 protein levels were measured at several time points after stimulation using immunoblotting. BMPR2 protein levels were normalized by GAPDH protein levels and the fold change from $t = 0$ was plotted. Error bars represent SD between 3 independent repeats. (G–J) The role of HSPGs was analyzed by inhibiting its biosynthesis using NaClO_3 (G) or by enzymatically removing HSPG using heparinase (H). Results with and without treatment show a high level of correlation around the line $y = x$ plotted in black in (I) and (J).

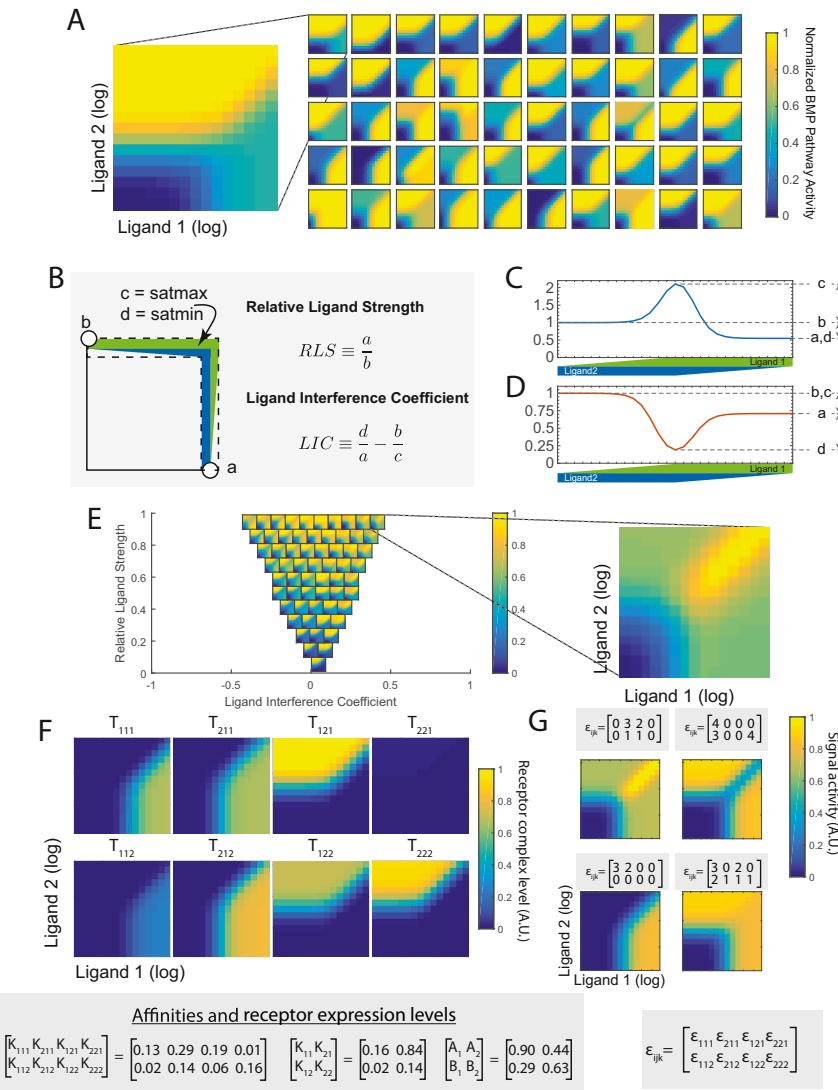


Figure S4. Analysis of Ligand Integration Functions in the Mathematical Model, Related to Figure 4

(A) Different biochemical parameter sets generate a range of 2-ligand integration functions. Here, we plotted the steady-state response for 50 randomly selected parameter sets (grid of heatmaps). These responses are not organized spatially. Note the broad range of behaviors and the general dependence on ratiometric features at high total ligand concentrations, reflected by the diagonal contours.

(B) 2-ligand response profiles can be parameterized by Relative Ligand Strength (RLS) and Ligand Interference Coefficient (LIC). These coefficients are determined by four activity levels that can be extracted from the high total ligand regime: the activity generated by the weaker (a) and stronger (b) ligands individually, as well as the maximal (c) and minimal (d) activity over the entire high ligand region, denoted by satmax and satmin, respectively.

(C and D) Determination of RLS and LIC for balance (C) and imbalance (D) detection.

(E) For each (LIC, RLS) coordinate pair, we computed the mean response functions for 5 biochemical parameter sets generating phenotypic parameters close to the indicated (LIC, RLS) point (location of heatmap). Inset zooms in on one specific (RLS, LIC) point.

(F and G) Activity parameters can produce distinct response profiles from the same set of affinity parameters. (F) For a specific set of K_{ij} , K_{ijk} values, indicated, the level of each trimeric signaling complex, T_{ijk} , is plotted as a function of the concentrations of two ligands. (G) The total pathway response depends in general on the levels of all trimeric complexes, each multiplied by a corresponding activity parameter. Here we plot 4 specific sets of activities (ϵ_{ijk}), each of which generates a distinct response profile, despite using the same affinity parameters.

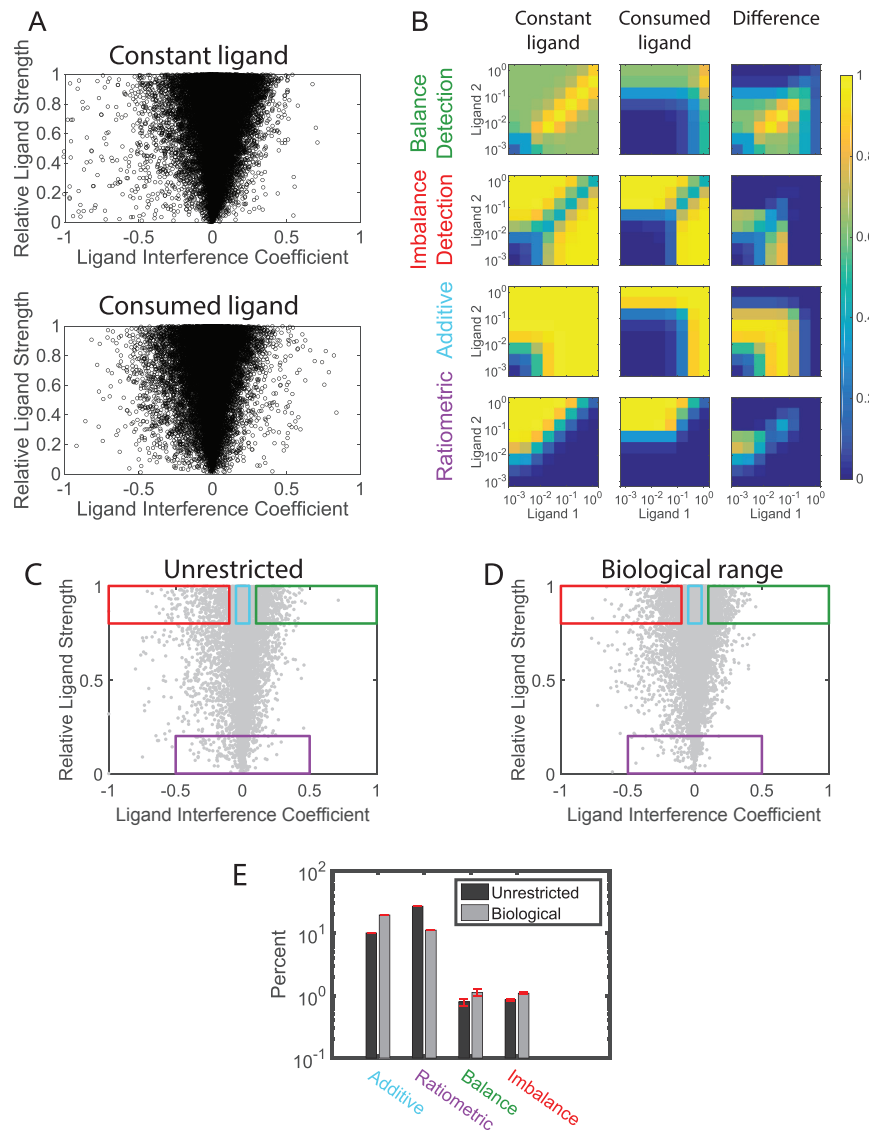


Figure S5. Changing Model Assumptions Has Mild Effects on Ligand Computations, Related to Figure 4

(A) 100,000 simulations were performed on randomly chosen parameter sets with (bottom) and without (top) allowing for consumption of ligands by cells. The calculated ligand interference coefficient and relative ligand strength (cf. Figures S4B–S4D) show similar distributions and produce all computations in both cases.

(B) Parameter sets corresponding to the 4 archetypes were selected and the full 2D input-output matrices are plotted for models with (center) and without (left) ligand consumption. The difference (right column) between the two models (constant ligand, left, versus consumed ligand, middle) demonstrate that the effects of ligand consumption are most significant at intermediate ligand levels, giving rise to a sharper signal response.

(C and D) 100,000 parameter sets were randomly selected either from the complete theoretically available parameter space, assuming a uniform distribution for the dimensionally reduced parameters (C) or from a biologically relevant range, based on previously measured values for BMP affinities (STAR Methods) (D). Resulting response profiles are plotted in the RLS-LIC space (see Figure S4). Specific regions in the neighborhood of each archetype are shown (colored boxes). (E) The percent of parameter sets giving rise to each response type is shown for the unrestricted parameter selection (black) and for parameters restricted to the biologically relevant range (gray). To estimate uncertainty, we calculated SD between 10,000 bootstrapped samples of size 100,000.

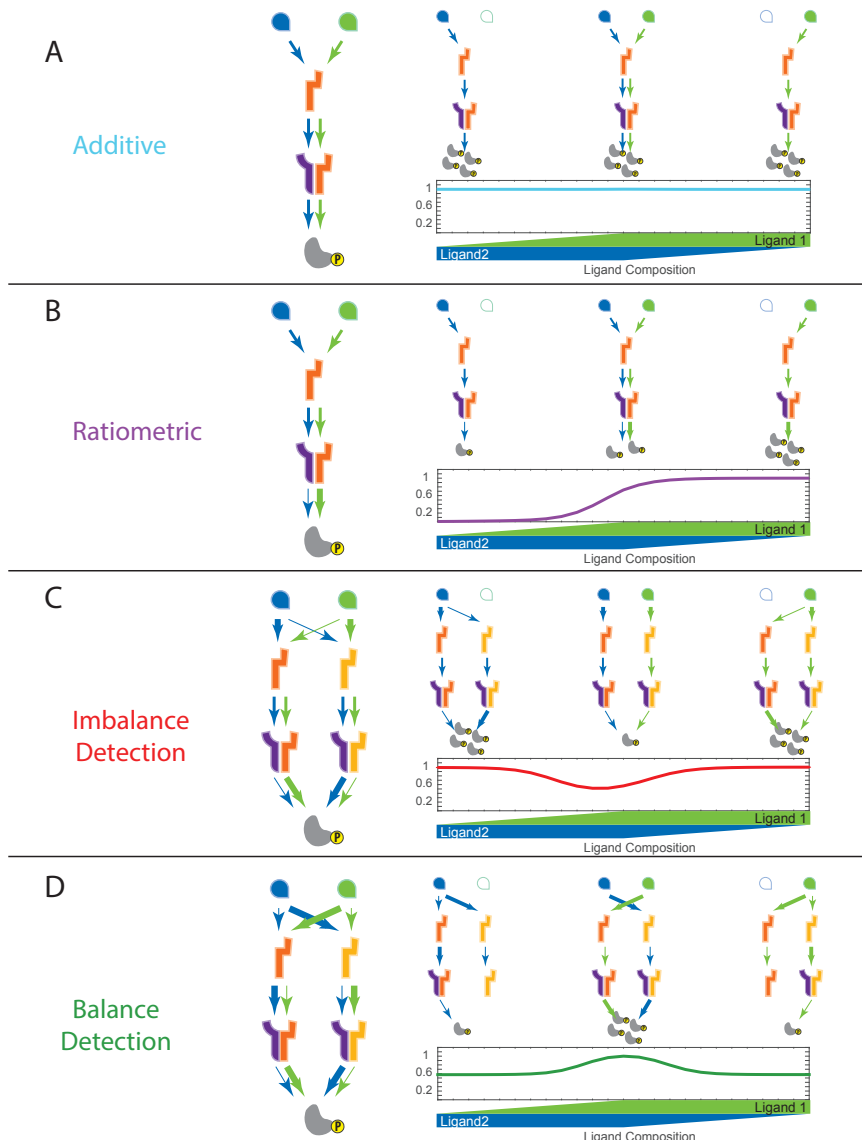


Figure S6. Archetypal Computations Emerge from the Interplay between Receptor Preference and Signaling Complex Activity in the Model, Related to Figure 5

For each archetypal computation (rows), the left-hand schematic represents a parameter regime sufficient for the computation (re-plotted from Figures 5A–5D). Arrow thicknesses represent the relative affinities or activities of indicated complexes. Arrow color represents the identity of the ligand in a given complex. To the right, the response profile across ligand compositions is shown (plot). The behavior of the system is also indicated schematically above the plot for three ligand composition regimes: only one ligand present (left and right) or an equal mixture of ligands (center). Hollow ligands represent those not present in each case. In each regime, some reactions do not occur (because a particular ligand is not present) or are disfavored (because of competition). Arrows for these reactions are omitted in the corresponding regimes. The total activity of the system in each of these three regimes is indicated by the number of copies of the phosphorylated second messenger.

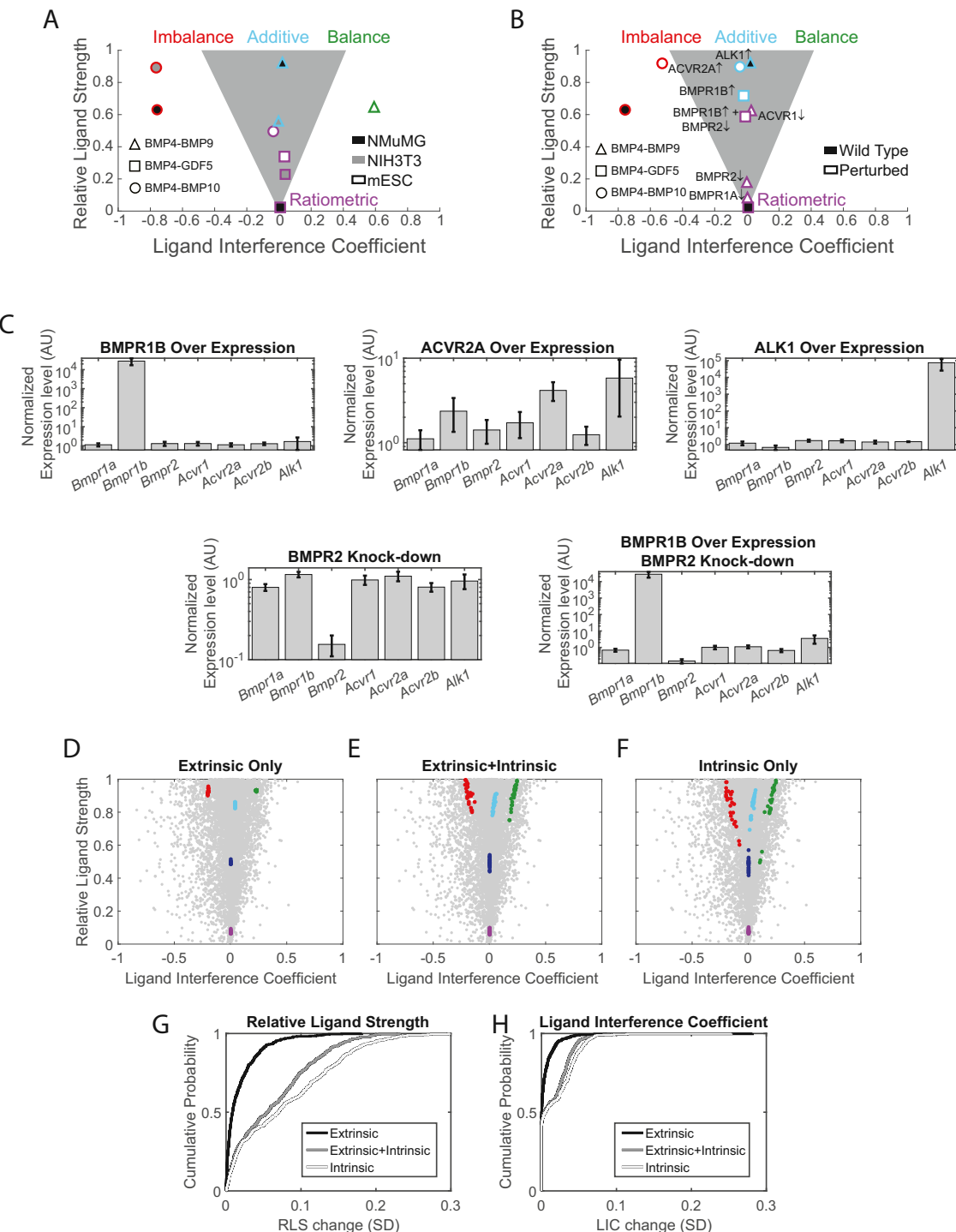


Figure S7. Receptor Expression Levels Reprogram Ligand Response Profiles, Related to Figure 6

(A) The relative ligand strength (RLS) and ligand interference coefficient (LIC) are plotted for each ligand pair (shape), for different cell lines (fill style). (B) RLS and LIC are plotted for each ligand pair (shape), for wild-type (filled), and each indicated receptor perturbation (hollow).

(C) Expression levels of all 7 BMP receptors in NMuMG cells were measured using qPCR, for each receptor perturbation (indicated) to quantify the effect size and specificity of knockdown or overexpression. Values represent fold expression relative to *Sdha* expression, relative to control cells, either wild-type (for receptor overexpression) or a non-specific siRNA (for receptor knock down). Error bars represent SEM from 4 independent measurements.

(D-F) Effects of noise in receptor expression on ligand integration mode. We analyzed the effects of noise on 5 specific parameter sets representing different response profiles (colors). For each parameter set, we analyzed 25 randomly perturbed receptor expression profiles chosen from a gamma distribution with a

(legend continued on next page)

coefficient of variation (CV) of 0.25. Each resulting interaction profile is plotted in the LIC-RLS phenotypic space. When the noise is extrinsic (correlated between all receptors) its effect in the phenotypic space is minimal, as shown by relatively small scatter of colored dots (D). Intrinsic noise (uncorrelated fluctuations in each receptor) increases the scatter (E and F).

(G and H) To generalize these results, we repeated the procedure in (D)–(F) for 100 parameter sets from each of the 5 regions (balance, imbalance, additive, ratiometric and intermediate regions). For each choice of receptor level, LIC and RLS parameters were calculated and the SD for the 25 choices was calculated. The cumulative distribution function of the SD in either the RLS (G) or LIC (H) is shown to indicate the distribution of sensitivities of ligand integration behavior to each category of noise.